TURUN YLIOPISTO
UNIVERSITY OF TURKU

SCANNING ELECTROCHEMICAL MICROSCOPY CHARACTERIZATION OF ENERGY MATERIALS

Mahdi Moghaddam

SCANNING ELECTROCHEMICAL MICROSCOPY CHARACTERIZATION OF ENERGY MATERIALS

Mahdi Moghaddam

University of Turku

Faculty of Technology
Department of Mechanical and Materials Engineering
Materials engineering
Doctoral programme in Technology (DPT)

Supervised by

Associate Professor, Pekka Peljo
University of Turku
Turku, Finland

Reviewed by

Associate professor
Antoni Forner-Cuenca
Eindhoven University of Technology
Eindhoven, The Netherlands

Associate professor
Edgar Ventosa
University of Burgos
Burgos, Spain

Opponent

Research group leader
Dr. Dmitry Momotenko
Carl von Ossietzky University of Oldenburg
Oldenburg, Germany

To my angels, maman and baba

تقدیم به نشانه های دوست، مامان و بابا

ABSTRACT

Replacing hydrocarbon-based energy production systems with alternative, low-carbon footprint ones is an urgent necessity. Advancing in this direction requires a thorough understanding of local electrochemical conversion and storage mechanisms at the interface of energy materials, which are key components of alternative energy systems. In this thesis, utilizing scanning electrochemical microscopy (SECM), novel insights are presented on two main groups of energy materials.

As for conversion, the presence of oxygen in electrocatalyst layers of polymer electrolyte membrane fuel cells was investigated. Using SECM in feedback mode, it was confirmed that co-existance of Nafion and carbon black leads to confinement of oxygen. It was suggested that oxygen is confined to the hydrophobic parts of self-assembled Nafion on the graphitic surfaces of the carbon black used as the catalyst support.

As for storage, charge transfer in solid active particles utilized as solid boosters for flow batteries was studied. First, the configuration where solid boosters are added to the tank of flow batteries was conceptualized. It was shown that the total accessible state of charge of the solid depends on the redox potential mismatch between the solid and the electrolyte. The smaller the mismatch, the higher the stored charge. In addition, it was shown that booster's available surface area is a critical technical requirement for operation of solid boosted flow batteries. In case of equal exchange current densities, the active surface area of the booster should be at least three times larger than that of electrode in the cell to drive the electrochemical reactions on the booster at a reasonable rate. Lastly, the behavior of copper hexacyanoferrate (CuHCF) booster microparticles was investigated at micro and nano scales combining SECM and optical microscopy. SECM tip was used, in a novel approach, as an optical mirror in addition to electrochemical triggering to enable mapping of the local conversion rates and states-of-charge, revealing a homogeneous surface conversion of nanocrystallites at short time followed by a slower heterogeneous bulk conversion. The heterogeneity is likely originating from locally different porosities or different nanocrystal size distribution.

KEYWORDS: Solid boosted flow battery, Scanning electrochemical microscopy, Redox mediation, Electrochemistry, Optical microscopy, Operando probing

TIIVISTELMÄ

Nykyisen hiilivetypohjaisen energiantuotantojärjestelmän korvaamisella vähähiilisillä vaihtoehdoilla on kiire. Tämä vihreä siirtymä edellyttää uusia energiamateriaaleja hyödyntäviä vaihtoehtoisia energiajärjestelmiä, ja uusien materiaalien kehitys edellyttää perusteellista ymmärrystä paikallisista sähkökemiallisista muunnos- ja varastointimekanismeista energiamateriaalien rajapinnoilla. Tässä työssä kehitettiin sähkökemiallista pyyhkäisymikroskopiaa sekä polttokennomateriaalien että akkumateriaalien tutkimiseen.

Työssä tutkittiin hapen läsnäoloa polymeerielektrolyyttimembraanipolttokennojen elektrokatalyyttikerroksissa. Sähkökemialliset pyyhkäisymikroskopiamittaukset vahvistivat, että Nafion-polymeerielektrolyytin ja hiilimustan seos kerää itseensä happea. Nafionin itsejärjestäytyy katalyyttikantajana käytetyn hiilimustan grafiittisille pinnoille muodostaen hydrofobisia eli vettä hylkiviä alueita, ja happi kerääntyy juuri näihin osiin. Tämä ilmiö pystyttiin osoittamaan sähkökemiallisella pyyhkäisymikroskopialla.

Akkumateriaalien osalta tutkittiin varauksen siirtoa kiinteissä sähkökemiallisesti aktiivisissa partikkeleissa, joita käytetään virtausakkujen kiinteinä sähkönvaraajina. Ensin määriteltiin konsepti, jossa kiinteä materiaali lisätään virtausakun säiliöön. Tällöin kiinteän aineen käytettävissä oleva kokonaisvaraustila riippuu potentiaalierosta kiinteän aineen ja elektrolyytin välillä. Mitä pienempi ero, sitä suurempi osa kiinteän aineen varauskapasiteetista on hyödynnettävissä. Lisäksi osoitettiin, että tankissa olevan kiinteän aineen aktiivisen pinta-alan tulee olla vähintään kolme kertaa suurempi kuin kennon elektrodin pinta-alan, jotta tankissa tapahtuvat sähkökemialliset reaktiot saadaan aikaan riittävällä nopeudella.

Lopuksi kiinteiden kupariheksasyanoferraatti -partikkelien käyttäytymistä tutkittiin mikro- ja nanomittakaavassa yhdistämällä sähkökemiallista pyyhkäisymikroskopiaa ja optista mikroskopiaa. Mittauseletrodikärkiä käytettiin uudessa lähestymistavassa sekä optisena peilinä että sähkökemiallisena elektrodina paikallisten konversionopeuksien ja lataustilojen kartoittamiseksi. Mittaukset osoittivat, että nanokiteiden pinnan konversion tapahtuu nopeasti, ja bulkkikonversio heterogeenisemmin ja hitaammin. Heterogeenisyys johtui todennäköisesti paikallisesti erilaisista huokoisuuksista tai erilaisesta nanokiteiden kokojakaumasta.

ASIASANAT: Kiinteät sähkönvaraajat, Sähkökemiallinen pyyhkäisymikroskopia, Varauksenvälitys, Sähkökemia, Optinen mikroskopia, Operando mittaus

Table of Contents

Abbreviations

ASR	Area-specific resistance
BET	Brunauer-Emmett-Teller analysis
BF	Bright field
BV	Butler-Volmer
CA	Chronoamperometry
CE	Counter electrode
CV	Cylclic voltammetry
CuHCF	Copper hexacyanoferrate
DF	Dark field
ET	Electron transfer
FB	Flow battery
GC	Glassy carbon
GDL	Gas diffusion layer
ITO	Indium tin oxide
MAE	Membrane electrode assembly
OCV	Open circuit voltage
ORR	Oxygen reduction reaction
PEM	Polymer exchange membrane fuel cells
Pt	Platinum
PBA	Prussian blue analogue
RDE	Rotating disc electrode
RE	Reference electrode
SB-FB	Solid boosted flow battery
SECM	Scanning electrochemical microscopy
SEM	Scanning electron microscopy
SHE	Standard hydrogen electrode
SI	Supporting information
SoC/SOC	State of charge
STEM	Scanning transmission electron microscopy
TEMPTMA	N,N,N-2,2,6,6-heptamethyl piperidinyl oxy-4- ammonium chloride
TPB	Three(Triple)-phase-boundary

UME	Ultra micro electrode
WE	Working electrode

List of Original Publications

This dissertation is based on the following original publications, which are referred to in the text by their Roman numerals:

I   **Mahdi Moghaddam**, Pekka Peljo. Oxygen absorption in electrocatalyst layers detected by scanning electrochemical microscopy. *ChemElectroChem*, 2021; 8: 2950-2955.

II   **Mahdi Moghaddam**, Silver Sepp, Cedrik Wiberg, Antonio Bertei, José Alexis Rucci, and Pekka Peljo. Thermodynamics, charge transfer and practical considerations of solid boosters in redox flow batteries. *Molecules*, 2021; 26: 2111.

III   **Mahdi Moghaddam**, Louis Godeffroy, Jerzy J. Jasielec, Nikolaos Kostopoulos, Jean-Marc Noël, Jean-Yves Piquemal, Jean-François Lemineur, Pekka Peljo, and Frédéric Kanoufi. Scanning electrochemical microscopy meets optical microscopy: probing the local paths of charge transfer operando in booster-microparticles for flow batteries. *Small*, 2023, submitted.

The original publications have been reproduced with the permission of the copyright holders.

List of related publications not included in the thesis:

D. Reynard, **M. Moghaddam**, C. Wiberg, S. Sepp, P. Peljo, and H. H. Girault, ''Chapter 5: Redox-mediated Processes'', Book chapter, Flow batteries: from fundamentals to applications, Wiley-VCH, 2023.

1   Introduction

Life is about positive contributions to help the other; to grow together to oneness; to overcome a great problem as a unity. One picks art, the other kindness, and another the science. All is opening a new window to let more light in; to enlighten what is around. This PhD thesis is an example of such a kind of contribution. It is a humble attempt towards untangling parts of a great challenge.

Among all major challenges humanity faces, climate change is undeniably one of the most significant, with *burning fossil fuels* for energy production as a major contributor. Numerous attempts are being made in various fields of science to mitigate the carbon footprint of energy production. In this regard, energy materials are at the center of attention as the building blocks of alternative energy systems replacing hydrocarbon-based systems. Either in seemingly well-established systems such as fuel cells or in cutting-edge concepts such as solid-enhanced flow batteries, understanding their intricate properties and behaviors is essential to optimize the performance or just to nurture an emerging conception.

Electrochemical characterization, where charge, potential, and current interplay, offers invaluable insights into charge transfer processes (electron and/or ion) and other underlying properties (catalytic activity for example) within energy materials.

At the outset of this thesis (**publication I**), a widely used electrocatalyst layer in polymer electrolyte membrane (PEM) fuel cells is studied as an energy conversion material. Scanning electrochemical microscopy (SECM) as the characterization technique provided valuable novel insights on beyond the conventional roles of graphitic surfaces and Nafion: their coexistence in catalyst layers result in gas absorption in the layer. This research showed hidden intricacies that can challenge commonly accepted practices for energy materials.

The remainder of the thesis shifts the focus onto solid active particles as energy storage materials. At first, an emerging configuration is conceptualized: solid active particles can be added to the tanks of conventional flow batteries to ''boost'' their energy density. Utilizing fundamental electrochemistry and physics, charge transfer in *solid boosted flow battery* (SB-FB) is formulated from the point of view of thermodynamics and kinetics. In addition, technical requirements (for example

overpotentials for electrochemical reactions) of such a configuration are investigated (**publication II**).

The interface between the redox active solid and the redox electrolyte involves a complex coupled ion-electron transfer. The final part of the thesis (**publication III**) comprehensively studies this interface, *operando* (under operating conditions), with copper hexacyano ferrate (CuHCF) as the booster. SECM is paired with optical microscopy in a novel approach: in addition to electrochemical triggering, the ultra micro electrode (UME) is used as an optical mirror enabling sub-micron spatial resolution imaging of solid particle conversion. It proposes a new methodology for better understanding of charge transfer not only for solid boosters but also for other solid active materials, involving intercalation/deintercalation processes, utilized in other configurations.

2 Electrochemistry simply explained

Electrochemistry is the study of the interplay between the flow of electrons, or simply electric current, and the chemical reactions with an external circuit being present between the reactants. An electrochemical reaction differs from a chemical reaction in that it involves the flow of electrons through an external circuit, unlike chemical reaction where electrons can transfer directly between reactants. In addition, electrochemical reactions can proceed, in an electrochemical cell, in either the forward or the reverse direction, depending on the conditions applied. In the following section, a brief review of fundamental electrochemical terms and concepts will be presented, drawing from widely recognized textbooks. [1,2]

An electrochemical cell in the simplest form is a *two-electrode setup*, as shown in **Figure 1**, which consists of two electrodes that are connected externally and are immersed in an electrolyte. In the cell, reactants go through either reduction or oxidation reaction or simply *redox* reactions, where one reactant, initially *red*, gives electrons to the external circuit at one electrode and will be oxidized to *ox*, and the other reactant, initially *ox'*, gains electrons from the external circuit at the other electrode and will be reduced to *red'*. The pair of the *red/ox* (or *red'/ox'*) species is known as a *redox couple*.

One electrode is the primary electrode where the electrochemical reaction under study occurs and is called *working electrode* (WE). The other electrode is called a *counter electrode* (CE). The CE, also known as the *auxiliary electrode*, provides a pathway for electrons to flow and complete the electrical circuit. The redox reactions taking place at each electrode are referred to as *half-cell* reactions. The sum of the half-cell reactions provide the overall cell reaction.
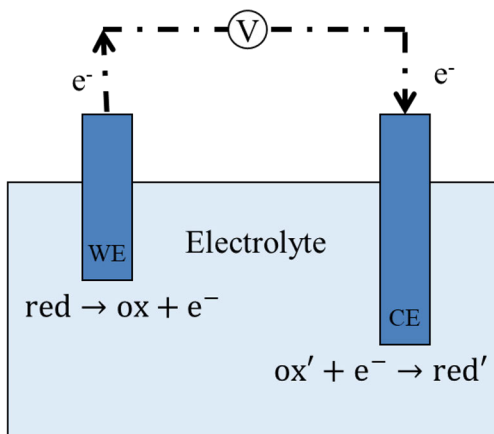
Figure 1. A two-electrode electrochemical cell.

The electric potential difference between the two electrodes is known as the *cell potential*. Similar to cell reaction that is the sum of half-cell reactions, the electromotive force, also called cell potential, is defined as the difference of the electrode potentials.

The electrode potentials are normally reported against a *reference* electrode whose potential is fixed. Based on conventions *standard hydrogen electrode* (SHE) is taken as the reference electrode in electrochemistry with the potential of 0 volts. When the potential of an electrode (i.e. the potential of the redox reaction of the chemical of interest taking place on the electrode) is measured in a two-electrode setup with the counter electrode being the SHE, the *standard potential* of the electrode (or of the redox reaction) is obtained being denoted with a 0 superscript (or subscript), E^0. Note that all the participants are in their standard states (unit activity) for the measurements i.e. 1 atm for gas phase, 1 M for solution, and ultimate purity for solids. Throughout this thesis, the standard values are mentioned with either a subscript or superscript 0.

2.1   Equilibrium: Nernst equation

In reality, the experiments in electrochemistry are not performed in standard conditions and activity of the participants is not unity. Let us assume that reaction (1) takes place on the WE and the activities are not unity:

$$ox + e^- \rightleftharpoons red \tag{1}$$

The potential of the electrode on which reaction (1) occurs is related to the activity of the *red* and *ox* species through *Nernst* equation as follows:

$$E = E^0 + \frac{RT}{F} \ln \left(\frac{a_{\text{ox}}}{a_{\text{red}}} \right) \tag{2}$$

where a is the activity, E^0 is the standard potential, F is the Faraday constant, R is the ideal gas constant, and T is temperature in Kelvin.

The Nernst equation provides the equilibrium potential of the electrode when there is no net current flowing through the electrode. It is the potential at which the rate of the oxidation and reduction reactions are equal and no current is externally being drawn from or supplied to the electrode. The backward (oxidation) and forward (reduction) currents of the reaction (1) are equal to the *exchange current density* (per unit area of the electrode), i_0, which is an intrinsic value.

2.2 Non-equilibrium: Butler-Volmer (kinetics) equation

In majority of the experiments, a potential is imposed on the WE to deviate it from the equilibrium towards the desired redox direction. The difference between the equilibrium potential and the imposed potential is known as *overpotential*, η. The magnitude of the overpotential influences on how fast the desired redox reaction occurs or simply how large the current flow would be in the electrode. The relationship between the current density and the overpotential is shown through the *Butler-Volmer* (BV) equation as follows:

$$i = i_0 (e^{\alpha f \eta} - e^{(\alpha - 1) f \eta}) \tag{3}$$

where i_0 is the exchange current density, $f = \frac{F}{RT}$, and α is a measure of the symmetry of the energy barrier for forward and backward directions of reaction (1) and is normally estimated as 0.5. The BV is the most important *kinetics* equation in electrochemistry. Note that in BV equation the effect of mass transfer limitation of the participants to and from the electrode is neglected meaning that they move fast enough that do not limit the overall redox reaction. In other words, it is assumed that negligible concentration gradients of the participants exist between the electrode surface and the bulk electrolyte. **Figure 2** shows the variation of the current density as a function of the overpotential based on equation (3) for $\alpha = 0.5$, $T = 298$ K, and $i_0 = 100$ A/m². The dotted lines show the oxidation or reduction components while the solid line shows the overall equation that is the sum of the oxidation and reduction components.
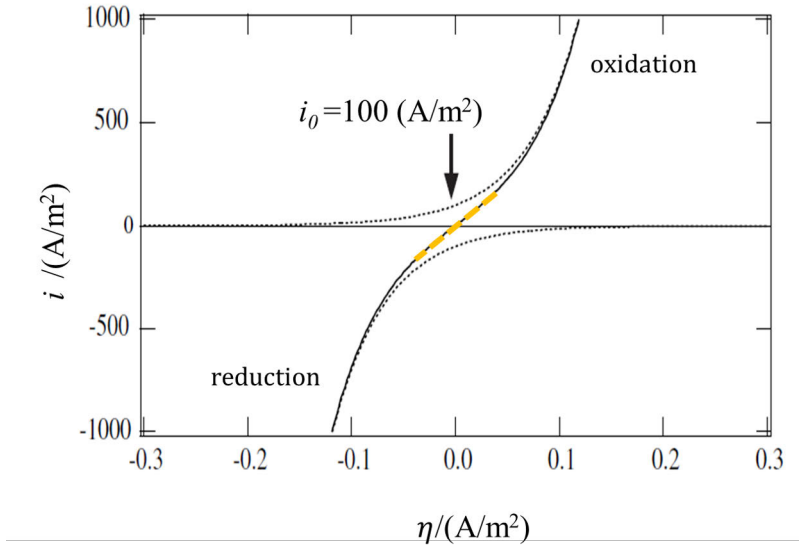
Figure 2. The variation of the current density as a function of the overpotential based on BV
equation (α = 0.5, T=298 K). Adapted figure.[2]

Large overpotentials in either direction make one of the components in the bracket
in equation (3) negligible. For example in case of large reductive (negative)
overpotentials, BV is simplified to equation (4):

$$i = -i_0 e^{(\alpha-1)f\eta}$$
$$(4)$$

However, in case of small overpotentials the exponential terms of BV are
approximated linearly ($x \ll 1,\ e^x = 1 + x$) and the equation (3) can be expressed
as follows:

$$i = i_0\, f\eta$$
$$(5)$$

Equation (5) is the *linearized form of BV* for small overpotentials near
equilibrium potential explained in 2.1. The yellow dashed line illustrates the linear
region of BV in **Figure 2**.

3   Energy Materials

As the demand for clean, reliable, and sustainable energy has been rising in the last few decades, the importance of energy materials has become evident more than ever before.[3–6] Some energy materials facilitate the conversion of energy from one type into another. For instance, the cathode materials, the membranes, and the catalysts used in fuel cells are energy conversion materials that facilitate the conversion of chemical energy stored in fuels, such as hydrogen, into electrical energy.[7–9] The other group of energy materials is employed to enable reversible storage of different types of energies for later use.[10] Liquid redox electrolytes that are utilized as the main energy storage material in conventional flow batteries, or solid redox-active materials that are employed as the energy storage medium in lithium-ion batteries, or in solid boosted flow batteries, are common examples of energy storage materials. They facilitate the conversion of electrical energy into chemical energy and vice versa.

3.1   Conversion

3.1.1   Electrocatalyst layers of PEM fuel cells

Fuel cells are electrochemical devices that convert chemical energy directly into electricity through electrochemical reactions, producing only water as a by-product. This makes them a compelling solution for reducing greenhouse gas emissions and dependency on fossil fuels.

Polymer (or Proton) Exchange Membrane (PEM) fuel cells are a type of fuel cell that use a proton conducting polymer electrolyte to separate the anode and the cathode. Nafion is the most commonly used proton conductive medium.[11–13] In a PEM fuel cell, the oxidation of the fuel, mostly hydrogen gas, produces protons and electrons at the anode. Produced electrons flow through the external electrical circuit to produce electricity, while protons (H^+) pass through the electrolyte membrane. Electrons and protons move to the cathode, where they interact with oxygen to produce water. **Figure 3** illustrates a simple overview of the operation of a PEM fuel cell.
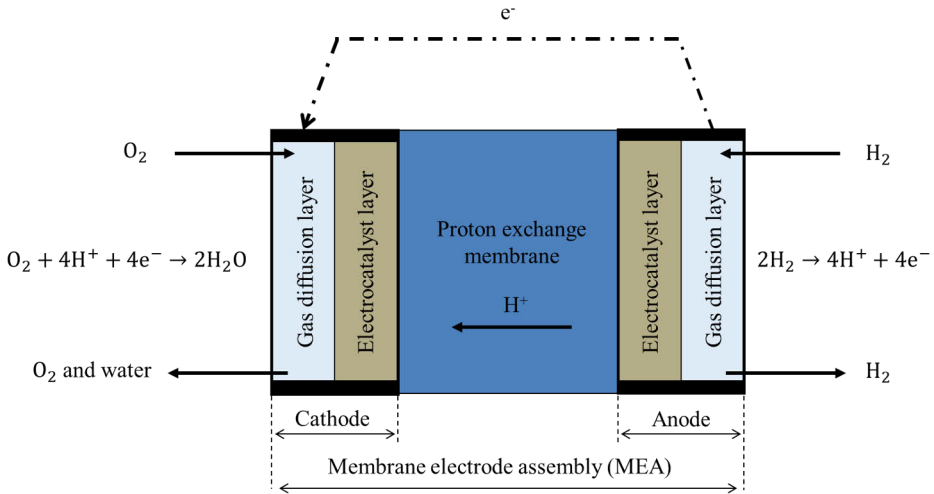
Figure 3. PEM fuel cell operation.

As shown in **Figure 3** each electrode consists of a gas diffusion layer (GDL) and an electrocatalyst layer. GDL is commonly a carbon-based porous material.[14,15] The assembly of the two electrodes and the electrolyte membrane is known as *membrane electrode assembly* (MEA).

While both sides of the PEM utilize electrocatalysts to facilitate the electrochemical oxygen reduction reaction (ORR) on the cathode or hydrogen oxidation reaction (HOR) on the anode, the cathode side is often more critical in terms of utilizing an electrocatalyst. The ORR tends to be the limiting factor in the overall performance of the PEM, necessitating efficient electrocatalysts to enhance its slow kinetics and the cell's overall efficiency.[13,16]

Figure 4 shows the structure of the cathode component of the MEA and the underlying gas and charge transfers. It is noteworthy that for GDL only conductive fibers are illustrated while in practice a carbon-based microporous layer is situated between the fibrous layer and the electrocatalyst layer.

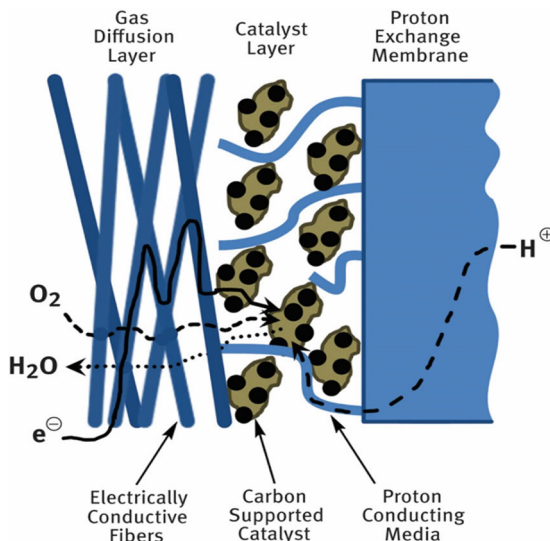**Figure 4.** Gas and charge transfer in the cathode of a PEM fuel cell. Reprinted with permission from reference.[12]

    The electrocatalyst layer is placed between the GDL and the membrane (**Figure 4**). It normally consists of three components: an electrocatalyst, an electron conductive support for the electrocatalyst, and a proton conductive ionomer. The electrocatalyst layer provides the so-called *three(or triple)-phase-boundaries* (TPBs) as the meeting points for electrons, protons, and reactant gases (i.e. O_2 in the cathode), at the electrocatalyst's surface.[13,17]

    Platinum (Pt) based electrocatalysts are shown to be the most effective catalyst for ORR.[12,13] As a common practice, Pt nano-particles are deposited on high surface area carbon powder known as the "catalyst support". Pt is expensive and efforts have been made within last decades to use as low loading as possible in electrocatalyst layers without compromising the efficiency and stability. In this regard, the electrocatalyst particles should be uniform and well dispersed on the support, forming the PEM cathode. Nafion ionomer has been widely employed for decades into the electrocatalyst layers, after its first successful incorporation in a PEM cell in 1986,[18] to extend the three-dimensional reaction zone, or TPB, and also to enhance the dispersion and uniformity of the electrocatalyst particles in the electrocatalyst layer.[19] Nafion as a proton conductive material facilitates the transportation of protons to the active sites of Pt nanoparticles inside the electrocatalyst layer. This feature is provided by the self-assembly of Nafion in aqueous media.[20–22] This self-assembly ensures sufficient ionic conductivity when an optimum amount of Nafion is present within the catalyst layer.[23–25]

3.1.2   Nafion self-assembly

Nafion structure consists of a hydrophobic part, a polytetrafluoroethylene backbone, and a hydrophilic part, perfluorinated-vinyl-polyether side chains that end with sulfonic acid. It self-assembles from the hydrophobic part on graphitic surfaces of the carbon support[26] (**Figure 5**) while its hydrophilic part serves as pathways of protons to the electroactive sites.[13]
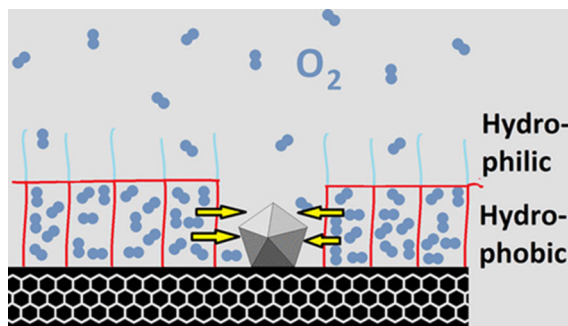

Figure 5.   Self-assembly of Nafion on graphitic surfaces of the catalyst's support. Oxygen can be confined within the hydrophobic parts. Reprinted with permission from reference.[26] Copyright 2016 American Chemical Society.

The presence of Nafion in catalyst layers is beneficial for catalysis efficiency.[13] However, the self-assembly of the ionomer may influence the catalysis efficiency. For instance, the self-assembly of Nafion around the electroactive sites might cause the spillover[27] effect. In this effect, either the backbone is imposed over the neighbouring catalytically active site, or sulfonic groups are adsorbed on the site. This effect impairs the activity of the site and leads to a lower catalytic activity than that of expected from a specific concentration of Pt.[26,27]

Another resulting effect is oxygen confinement in hydrophobic parts of self-assembled Nafion that is of interest for investigation in this work. Chlistunoff and Sansiñena discussed for the first time the novel concept of Nafion-induced oxygen confinement.[26,28] They reported that oxygen could be confined within the hydrophobic part of the self-assembled ionomer on the graphitic surfaces of the carbon support in aqueous media.

Oxygen confinement has so far been studied with rotating disk electrode (RDE) and cyclic voltammetry (CV).[26] In **publication I**, scanning electrochemical microscopy (SECM, refer to 4.1) is utilized in the feedback mode as the characterization technique to investigate the presence of oxygen in the Nafion-containing catalyst layers. SECM offers a rather less complicated configuration compared to RDE measurements of electrocatalyst layers.

3.2   Storage

Renewable energy integration into the power grid necessitates reliable and efficient large-scale energy storage solutions. Flow batteries (FBs) have emerged as a promising technology for stationary energy storage, offering scalability, extended cycle life, and the unique capability to decouple energy and power.[29,30]

In a FB the energy is stored within the dissolved redox couples in the liquid electrolytes that flow between the power cell and the tanks. The electrolyte in one tank contains a redox couple with relatively more positive Nernst potential and the other electrolyte contains another redox couple that has a more negative Nernst potential relative to the redox couple in the positive side. An ion-permeable membrane in the cell keeps the positive and the negative sides separate from each other. Electrodes in positive and negative sides in the cell are externally wired and electrons flow between the electrodes while charging or discharging the battery. **Figure 6** depicts a FB setup during charge.
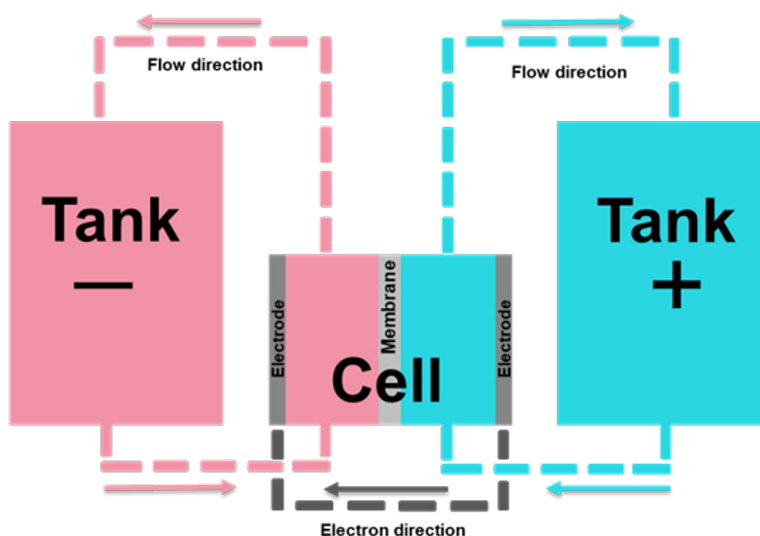
Figure 6. A flow battery setup. The electron direction is shown during charge.

During charge, the redox couple in the positive side is oxidized while the redox couple in the negative side is reduced. To charge the battery, electrochemical reactions are electrolytic (non-spontaneous). During discharge, reverse reactions that are galvanic (spontaneous) take place to provide electric energy in the external circuit. The theoretical overall cell potential is the difference between the redox (Nernst) potentials of the redox couples in the positive and negative sides.

Numerous chemistries are found in the literature for operation in a FB but prominently vanadium systems have reached production scales.[29–33] Nevertheless, vanadium is not an abundant element and its availability along with its cost is appearing as a great hindrance for vanadium-FBs. In addition, the relatively low energy density of FBs remains a limitation, impeding their widespread deployment.[30,34] Alternative concepts are essential to overcome these limitations. Solid boosted flow battery (SB-FBs), introduced in 3.2.1, is an alternative concept that is studied in this thesis.

3.2.1   Solid boosters in flow batteries

Conventionally, FBs rely on the redox-active species dissolved within the liquid electrolyte. Therefore, the charge storage is inherently constrained by the solubility of the redox species in the electrolyte, limiting the energy storage density of the system. Solid boosted flow batteries (SB-FBs) present an alternative paradigm, where redox-active solid particles are introduced into the tanks of the battery. The dissolved redox couples within the electrolyte act as charge transfer mediators to deliver the charge to the confined solid particles. Consequently, the redox solid material becomes the primary contributor to energy storage. Unlike the conventional reliance on the solubility of redox species in the electrolyte, the SB-FB benefits from the intrinsically higher volumetric charge storage density of the redox solid material compared to that of the electrolyte that results in enhanced energy density of the battery.

Figure 7 shows a flow battery with TEMPTMA (N,N,N-2,2,6,6-heptamethyl piperidinyl oxy-4- ammonium chloride) redox couple dissolved in the positive electrolyte and Zn^{2+}/Zn redox couple dissolved in the negative electrolyte with 1 M KCl as the supporting electrolyte. Copper hexacyanoferrate (CuHCF) solid particles are added to the positive tank.
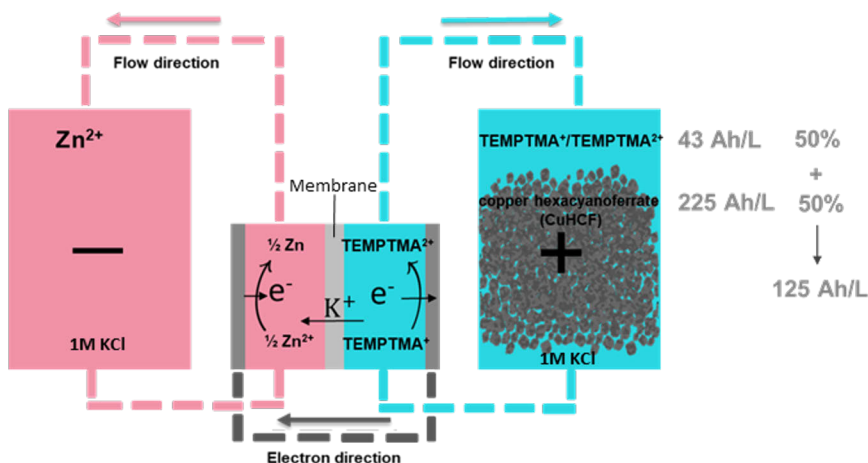
Figure 7. A solid boosted flow battery with CuHCF solid boosters in the positive side.

This configuration is called a *solid boosted flow battery* and CuHCF is referred to as *solid booster*. The solid booster can be charged and discharged through TEMPTMA. As shown in **Figure 7**, during battery's charge, TEMPTMA$^+$ is oxidized to TEMPTMA^{2+} in the cell in the positive side with giving an electron to the external circuit. The electron travels through the external circuit to the negative side to reduce ½ Zn^{2+} to ½ Zn. TEMPTMA^{2+} is then pumped to the tank. In the tank, the reverse reaction takes place on the solid booster's surface and TEMPTMA^{2+} is reduced back to TEMPTMA$^+$ while the solid booster itself is oxidized from an initial reduced state by losing an electron and in addition, a cation deintercalates from its bulk structure. **The contact of the electrolyte and the solid is the interface where thermodynamics and kinetics (dynamics) of the charge transfer are studied in this work.** TEMPTMA$^+$ is then pumped to the cell and it is re-oxidized to TEMPTMA^{2+} and the cycle continues until the battery is fully charged. It is shown that addition of 50 vol-% of CuHCF results in a 3-fold improvement (125 Ah/L) in the charge storage density of the battery in comparison with a system with no solid particle in the tank (43 Ah/L).[35]

The charge transfer within SB-FBs takes place on a distinctive interface between the solid particles and the redox electrolyte. The charge transfer is a coupled electron-ion transfer. A comprehensive understanding of the thermodynamics and kinetics/dynamics governing this charge transfer process is essential for optimizing the design and operation of SB-FBs.

The formulation of operation of SB-FBs from thermodynamics and technical points of views were missing, scarce or scattered in the literature until recently. To fill this gap in **publication II** the theoretical thermodynamics of electrochemical charge transfer in such systems is characterized based on Fermi level equilibration

and technical aspects are studied based on the kinetics governing the charge transfer in the tank and in the cell.

The kinetics/dynamics of the coupled electron-ion transfer on the surface of the solid booster is relatively neglected in the literature due to its inherent complexity.[35–40] In **publication III** the dynamics of charge transfer between CuHCF as the solid booster and TEMPTMA as the redox electrolyte is studied. During charge and discharge, CuHCF goes through optical absorption variations that are detectable in the opto-electrochemical SECM setup. The setup enables probing the redox-mediated conversion mechanism of CuHCF micro particles *operando* at sub-micron spatial resolution.

3.2.1.1   Redox mediation history

The solid booster concept known as the ''Redox Targeting System'' or ''Redox Mediated Process'' was initially proposed by Wang et al. in 2006.[41] Their research demonstrated the ability to charge and discharge a redox-active solid, $LiFePO_4$, using two different osmium complexes as redox couples with higher and lower potentials, respectively, than the solid material. Building upon this concept, subsequent studies explored the use of different redox mediators to enable redox targeting of other solid materials. For example, ferrocenes were employed as mediators for $LiFePO_4$,[42] while cobaltocenes were used for redox targeting of Li_xTiO_2.[43] In 2016, a battery was introduced featuring a solid Li anode, physically separated from the non-aqueous electrolyte by a lithium-conducting medium. This setup allowed for the redox targeting of $LiFePO_4$ with iodide.[44,45] In 2017, Zanzola et al. introduced the concept of "Redox Solid Energy Boosters".[46] They demonstrated the effectiveness of a single redox couple coupled with a solid storage material. The aqueous system contained the $Fe^{3+/2+}$ redox couple in an acidic chloride electrolyte, paired with polyaniline as the solid material. This configuration resulted in a three-fold enhancement in energy storage capacity and significant improvement of the voltage efficiency. Recently, other studies have investigated single redox electrolyte systems paired with different solid boosters, including copper hexacyanoferrate,[35] $Ni(OH)_2$,[47] Prussian blue,[48] and polyimide.[49] As a recent study, the thermodynamics and kinetics of $LiFePO_4/FePO_4$ as the solid material and $[Fe(CN)_6]^{4-/3-}$ as the redox mediator were investigated. By adjusting the redox potential of the electrolyte using dimethylsulfoxide as cosolvent, utilizing a low current density of 0.25 mA/cm^2, and employing a highly porous solid material, near-theoretical capacity utilization was achieved with a coulombic efficiency of 99%.[36] These works have provided insights into the potential of solid boosters for enhancing the energy density in flow batteries. For further reference, a comprehensive review on flow batteries with solid boosters has been published recently.[50]

3.2.1.2   Fermi level equilibration in redox mediation

The Fermi-Dirac statistics, built upon the Pauli exclusion principal, predict the electron's statistical behavior and provide the probability of electrons occupying different energy levels in a system at a given temperature. E_F, the Fermi level is the highest energy level at which an electron can exist at 0 K. No electrons are found at energy levels higher than E_F. With increasing the temperature, the probability acquires values other than 1 or 0 around the E_F where the probability remains always as 0.5.
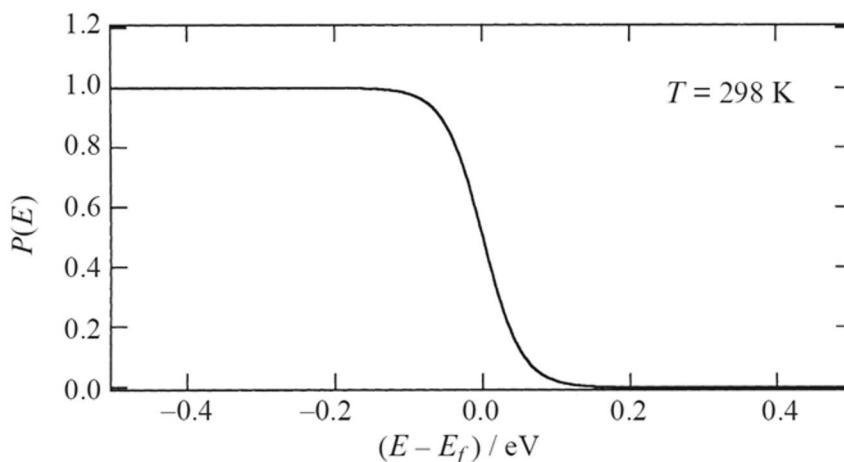
Figure 8. The Fermi-Dirac distribution function.[2]

The Fermi level of a phase is defined as the electrochemical potential of electrons in that phase:[1]

$$E_F = \tilde{\mu}_{e^-} \tag{6}$$

The electrochemical potential of species i in a phase is defined as the energy that is required to bring one mol of species i from vacuum, as the zero reference point, into the phase:

$$\tilde{\mu}_i = \mu_i + z_i F \phi = \mu_i + z_i F (\chi + \psi) \tag{7}$$

Part of the work, μ_i, known as chemical potential, is attributed to the chemical interactions and the other, ϕ, known as inner potential, is attributed to the electrostatic interactions during transferring the ions. The electrostatic part itself is divided into two; the outer potential, ψ, which is associated with the charge on the

phase, and the interface potential, χ, which is associated with the interactions of the species with the interface while crossing it. z_i is the charge of the species i and F is the Faraday constant.

For a solid with electron conductivity, the Fermi energy is defined as the energy that is required to bring one mol of electrons from vacuum wherever into the phase:

$$E_{F,s} = \tilde{\mu}_{e^-} = \mu_{e^-} - F\phi = \mu_{e^-} - F(\chi + \psi) = \alpha_{e^-} - F\psi \tag{8}$$

If the charge on the surface of the phase is zero ($\psi = 0$), the Fermi energy by definition is equal to the real chemical potential of the electron in the phase, α_{e^-}. Note that work function, the work to remove an electron from an uncharged solid, is by definition $-\alpha_{e^-}$. The real chemical potential is an intrinsic parameter for solids depending on the electronic structure and atomic scale surface conditions.[2]

In a redox solution however, the situation is different. The solution contains both oxidized and reduced species; hence, the electrochemical potential of electrons in the solution depends on both species. By definition, the electrochemical potential of electrons in a liquid redox solution is the difference of electrochemical potentials of the reduced and oxidized species:[1,30,51]

$$E_{F,l} = \tilde{\mu}_{e^-} = \tilde{\mu}_{red} - \tilde{\mu}_{ox} \tag{9}$$

Based on equation (9) and employing the equation (7) with an analogy to the Nernst equation, the Fermi level of electrons in a solution is given as follows:

$$E_{F,l} = \tilde{\mu}_{e^-} = -F(\phi + E_{ox/red}) \tag{10}$$

where $E_{ox/red}$ is the absolute value of the redox potential of the electrolyte (vacuum as reference point). If the Standard Hydrogen Electrode (SHE) is used as the reference, the equation (10) is redefined as follows:

$$E_{F,l} = \tilde{\mu}_{e^-} = -F(\phi + [E_{ox/red}]_{SHE} + 4.44 \pm 0.05 \text{ V}) \tag{11}$$

When two phases are in contact, electrons from the phase with a higher Fermi level should move to the one with a lower energy based on the thermodynamics. At equilibrium the electrochemical potentials of the two phases, and therefore the Fermi level of the two phases become equal. Nevertheless, kinetics limitations might prevent the system from reaching the equilibrium.

In the tank of a SB-FB, the redox active solid is surrounded by the liquid redox electrolyte with which it should equilibrate electrochemically. Electrons transfer from the Fermi level with higher energy to the one with lower energy until the Fermi

levels of the electrolyte and the solid equilibrate ($E_{F,s} = E_{F,l}$). Depending on the state of charge, the Fermi level with higher energy could be either the solid or the electrolyte. It is noteworthy that the electron exchange between the solid and the electrolyte is coupled with cation de/intercalation from/into the redox solid for the sake of charge neutrality in the bulk of solid.

4   Electrochemical characterization

4.1   Scanning Electrochemical Microscopy (SECM)

Scanning electrochemical microscopy (SECM) is a scanning probe technique with relatively high spatial and temporal resolution. Since its introduction by Bard in 80s, it has been employed in various fields of biochemistry, corrosion, catalysis, and energy to study surface reactivity and electron transfer reactions.[52,53]

The key difference in electrochemical measurements done by SECM results from the minimal active area of the working electrode (WE) with the disc-shaped tip that ranges from a few to tens of micrometers and is widely known as Ultra Micro Electrode (UME).[1] UME is a micrometer diameter wire of a conductive material (Pt, Au, C, etc.) embedded in a non-conductive sheath with glass as the most commonly used material for the sheath. The disc-shaped tip therefore consists of a central active area (e.g. Pt) surrounded by an inactive area (e.g. glass). Ratio of the inactive radius over the active radius is known as R_g and is normally around 10. The sheath radius should be large enough to include the hemispherical diffusion field around the active area but still not too large to impose long distances for lateral diffusion of R species to the active area when the tip is close to the surface. Too large or too small sheath around the central active area would lead to lower sensitivity of the SECM experiment.[54–57]

The small dimensions of the tip of the WE enables to locate/scan it at the vicinity (a few microns away) of an electrolyte-immersed substrate. The current at the tip is influenced by the physicochemical properties of the substrate such as roughness, redox activity, electrochemical reactivity, and conductivity. The tip current is also influenced by whether the conductive substrate is electrically biased or not. As it will be discussed in the following sections, the amplitude and the profile of the tip current (which is customarily presented vs the tip distance from the substrate) in time or potential dependent measurements provide key information on the material under study as the substrate.[53,56]

4.1.1   Feedback mode

SECM *feedback mode* is the most practiced mode of measurement in different fields where SECM is utilized. In **publication I**, scanning electrochemical microscopy is utilized in the feedback mode as the characterization technique to investigate the presence of oxygen in the Nafion-containing catalyst layers. In this mode, the potential at which ORR occurs is applied to the tip (the tip is biased) and the tip approaches the unbiased substrate. In **publication III**, SECM feedback mode is paired with optical microscopy to study the dynamics of charge transfer between CuHCF as the solid booster and TEMPTMA as the redox electrolyte. The tip that is biased for the redox potential of TEMPTMA locates a few microns away from the substrate, which is a CuHCF single particle, to trigger its charging and discharging via TEMPTMA. Meanwhile the tip current is studied in the transient condition. The feedback mode in transient conditions is also referred to as surface interrogation SECM (SI-SECM).[55]

In general, in the feedback mode the tip is biased with a potential at which a desired redox reaction takes place:

$$R_{(aq)} \rightarrow O_{(aq)} + e^-$$
(12)

When the tip is far away from the substrate, generally greater than a few times the radius of the tip's central electroactive area, a, the tip current is known as bulk or steady state current (i_{T_∞}). The diffusion of dissolved R species to the tip limits the bulk current shown in equation (13):[56,57]

$$i_{T_\infty} = 4nFDaC \, \beta(R_g)$$
(13)

where F is the Faraday constant, D is the diffusion coefficient of the R species, a is the radius of the tip's central active area, C is the bulk concentration of R species, and β is a function of R_g which is around 1 for $R_g \geq 10$.

In the feedback mode, the tip current is recorded while the biased tip is either located close to the substrate (the case in **publication III**) or is approaching the substrate (the case in **publication I**). When the tip is closer than a few times a to the substrate, the substrate starts to disrupt the hemispherical diffusion field of dissolved $R_{(aq)}$ species to the tip. The closer the tip gets to the substrate, the more the diffusion is hindered due the substrate blockage.

The resulting profile of the current depends on the nature of the substrate and typically two opposite responses can be observed. If the substrate material is insulating and redox inactive, approaching of the tip to the substrate leads to a decrease in the tip current (i_T) compared to the bulk (i_{T_∞}). This response is known as the *negative feedback*.

On the other hand, if the substrate is able to reverse the equation (12) (i.e. the substrate is conductive, is redox active, or holds R species in its structure) fresh $R_{(aq)}$ species are supplied by the substrate and the current is increased compared to the bulk current. This response is known as the *positive feedback*. In this case the produced $O_{(aq)}$ species at the tip are reduced back to $R_{(aq)}$ on the substrate and diffuse back to the tip leading to an increased current at the tip.

In case of a redox active substrate, such as thin-films or a single particle of battery materials (**publication III**), $O_{(aq)}$ species are reduced back to $R_{(aq)}$ on the substrate while the substrate itself goes through a separate redox reaction, giving electrons to $O_{(aq)}$ species:

$$R_{(s)} \rightarrow O_{(s)} + e^- \tag{14}$$

With the loop of reproducing $R_{(aq)}$ on the substrate, the tip current increases when the tip locates close to or approaches the redox active substrate exhibiting a positive feedback response. Numerous examples of positive feedback response in different systems are observed in the literature but all of them follow the same principle of regeneration of $R_{(aq)}$ species at the substrate and reverse diffusion to the tip.[58–60]

4.1.2   SECM approach curve

In SECM measurements customarily the collected tip current (i_T) is normalized by dividing it with the bulk current previously shown in equation (13):

$$I_T = i_T / i_{T_\infty} \tag{15}$$

I_T is shown vs the tip distance L that is normalized by dividing the actual tip to substrate distance (d) with radius of central active area of the tip (a):

$$L = d/a \tag{16}$$

I_T-L is widely known as the *approach curve*. **Figure 17** and **Figure 18**, as the experimental results of **Publication I**, are examples of approach curves.

Current responses in feedback mode measurements for different systems can be placed somewhere between two extreme situations of positive and negative feedback. A feedback that is not purely negative or positive can be referred to as a mixed response.

Lefrou and Cornut have published a great review gathering all the analytical expressions for quantitative SECM.[57] For the first time they included R_g (ratio of the

inactive radius over the active radius of the tip) in the analytical expression for positive and negative feedback. [61–63] Formerly, expressions only included L.

The approximate expression for the negative feedback for an UME with disc shape tip and finite R_g is shown in equation (17):

$$
\begin{aligned}
I_{NF}&(L, R_g) \\
&= \left[\frac{2.08}{R_g^{0.358}} \left(L - \frac{0.145}{R_g} \right) + 1.585 \right] \\
&\quad \times \left[\frac{2.08}{R_g^{0.358}} (L + 0.0023 R_g) + 1.57 + \frac{\ln R_g}{L} \right. \\
&\quad \left. + \frac{2}{\pi R_g} \ln \left(1 + \frac{\pi R_g}{2L} \right) \right]^{-1}
\end{aligned}
\tag{17}
$$

and for the positive feedback is shown in equation (18):

$$
\begin{aligned}
I_{PF}(L, R_g) &= \alpha(R_g) + \frac{1}{\beta(R_g)} \frac{\pi}{4 \mathrm{ArcTan}(L)} \\
&\quad + \left(1 - \alpha(R_g) - \frac{1}{2\beta(R_g)} \right) \frac{2}{\pi} \mathrm{ArcTan}(L)
\end{aligned}
\tag{18}
$$

where α and β are functions of R_g and are obtained as follows:

$$
\begin{aligned}
\alpha(R_g) &= \ln 2 + \ln 2 \left(1 - \frac{2}{\pi} \mathrm{ArcCos}(\frac{1}{R_g}) \right) \\
&\quad - \ln 2 \left[1 - \left(\frac{2}{\pi} \mathrm{ArcCos}(\frac{1}{R_g}) \right)^2 \right]
\end{aligned}
\tag{19}
$$

$$
\begin{aligned}
\beta(R_g) &= 1 + 0.639 \left(1 - \frac{2}{\pi} \mathrm{ArcCos}(\frac{1}{R_g}) \right) \\
&\quad - 0.186 \left[1 - \left(\frac{2}{\pi} \mathrm{ArcCos}(\frac{1}{R_g}) \right)^2 \right]
\end{aligned}
\tag{20}
$$

5   Experimental

5.1   Materials

In **publication I**, the catalyst, nominally 20 wt-% Pt on carbon black was purchased from Alfa Aesar. Timcal Super C65 was utilized for samples containing carbon black. Nafion 115 Dupont membrane was purchased from Ion Power and the 5 wt-% Nafion solution was purchased from Sigma Aldrich. The UME electrode was prepared in-house with a platinum tip radius of a=12.5 μm and Rg=8.

In **publication III**, ITO-coated glass coverslips (thickness #1.5) with a resistivity of 15-30 Ω.cm were purchased from SPI. TEMPTMA was provided by the group of Prof. Hubert Girault at EPFL. The synthesis steps has been previously reported.[64] CuHCF was synthesized in-house according to a previously reported procedure.[35] The Pt UME, used as the working electrode was prepared in-house using a borosilicate glass capillary (Sutter Instrument) with outer and inner diameters of 1.0 and 0.5 mm, respectively. A 12.5 μm radius Pt wire (99.99%, annealed, Goodfellow) was inserted into the capillary and sealed with a P-2000 Sutter Instrument laser puller.

5.1.1   Copper hexacyanoferrate (CuHCF)

5.1.1.1   Structure

CuHCF is a Prussian blue analogue (PBA). PBAs' crystal framework is shown in **Figure 9 a** where Fe (II) nitrogen coordinated sites in the original Prussian blue structure are replaced by other transition metals (Cu, Mn, Ni, Co, and Zn) shown as M (II).[65–69] Sub-cubes within the crystal lattice can accommodate hydrated alkali cations, such as sodium or potassium. The process of intercalation and deintercalation of these cations is responsible for the rechargeable nature observed in these structures. CuHCF is analogous to Prussian blue with having copper (II) as the transition metal in the nitrogen coordinated sites. K^+ ions locate in the tetrahedrally coordinated sites within the sub-cubes. **Figure 9 b** shows the crystal structure of CuHCF and the intercalation/deintercalation reaction. Galvanostatic cycling of CuHCF in 1 M KNO_3 and 0.01 M HNO_3 is shown **Figure 9 c**.
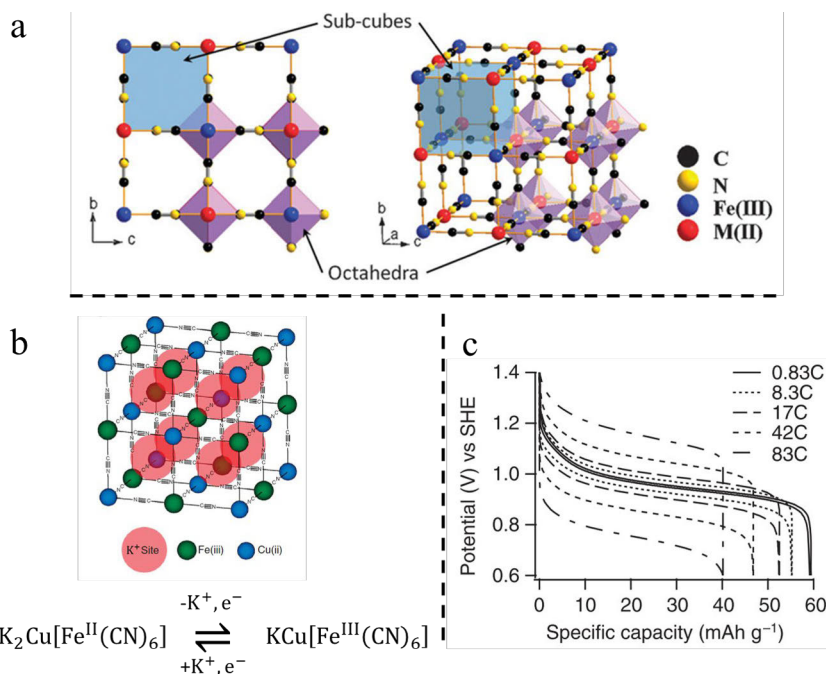
Figure 9. Structure and cycling of CuHCF. **a)** general structure of PBAs. Reproduced from reference with permission from the Royal Society of Chemistry.[68] **b)** CuHCF structure and K+ intercalation/deintercalation reaction (adapted).[69] **c)** galvanostatic cycling of CuHCF in 1 M KNO₃ and 0.01 M HNO₃.[69] Adapted with permission from Springer Nature.

5.1.1.2   Synthesis

Copper hexacynoferrate was synthesized, as previously reported,[35] by gradual and simultaneous pumping of 120 mL of 0.1 M copper (II) nitrate trihydrate and 120 mL of 0.05 M potassium ferrocyanide trihydrate from two separate beakers to a third one containing 60 mL of Milli-Q water under magnetic stirring. The obtained suspension was then centrifuged three times for 30 minutes with removing the solution between each round. The suspension was allowed to rest for couple of hours after which the sedimentation was collected in the form of slurry through filtering and washing with Milli-Q water. The slurry was dried under vacuum at room temperature overnight to obtain pristine CuHCF agglomerates.

5.2   Methods

5.2.1   SECM of electrocatalyst layers

The SECM setup utilized in **publication I**, shown in **Figure 10**, is composed of a PTFE cylindrical chamber with diameter and height of 15 mm, with a removable

glassy carbon (GC) electrode with a radius of 2.5 mm (0.1 in) at the bottom. The CHI900 SECM Bi-potentiostat with an integrated positioning system is employed for electrochemical measurements. An in-house prepared silver/silver chloride double junction electrode and a Pt wire were used as reference and counter electrodes, respectively, in a three-electrode configuration. The whole setup was placed inside a Faraday cage during measurements.
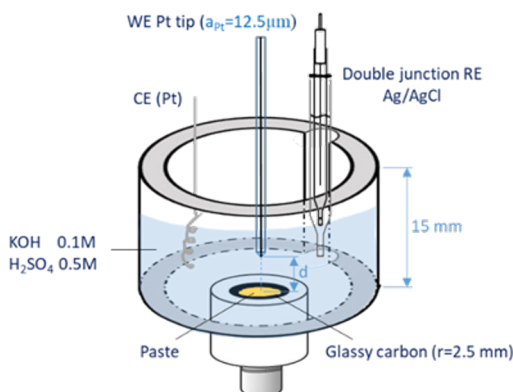

Figure 10. SECM setup for studying electrocatalyst layers.[1]

5.2.1.1 Ink preparation and drop-casting

The catalyst ink was prepared by adding 5 mg of 20 wt-% Pt on carbon black to 1.3 ml solvent mixture consisting of 80 vol-% water and 20 vol-% 2-propanol. The dispersion was then stirred for 30 minutes, followed by 15 minutes of sonication, and an additional 30 minutes of stirring to achieve ink homogenization. For drop-casting, 5 µl of the ink was pipetted onto the GC at a density of 0.1 mg/cm^2 and allowed to dry in the ambient atmosphere. An additional 5 µl of the ink was then applied on top of the dried ink layer to reach a final concentration of 0.2 mg/cm^2 of solid.

As for the carbon black ink, it was prepared by combining 4.4 mg of carbon black with 260 µl of a solvent solution comprising 80 vol-% water and 20 vol-% 2-propanol. The carbon black ink was mixed with Nafion in two different ratios of 1 wt-% and 47 wt-% each used as a separate sample. Subsequently, the Nafion-mixed carbon black inks were drop-casted on the GC surface, reaching a final concentration of 0.86 mg/cm^2 of carbon.

5.2.2 UME-mirrored epi-illumination microscopy

The UME-mirrored epi-illumination (where illumination is implemented via the objective lens) setup utilized in **publication III** is shown in **Figure 11**. The CuHCF-drop-casted ITO substrate was mounted on a motorized inverted optical microscope (Axio Observer 7, Zeiss) and illuminated from the bottom by means of an unpolarized white light source through a 63x oil immersion objective (Plan Apochromat, Zeiss) with a numerical aperture of 1.4. An ElProScan electrochemical probe scanner from Heka with a three-axis piezo stage and a low-noise PG 618 ultra bipotentiostat was mounted on top of the optical microscope and used to approach the Pt UME above the substrate. The light reflected by the substrate and the Pt UME was collected by a CMOS camera (Axiocam 705 color, Zeiss). The Pt UME was used as the working electrode and Pt wire was used as the counter electrode in a two-electrode configuration. The potentiostat was synchronized with the digital camera by a signal generator. The whole setup was placed inside a Faraday cage. The setup is located at *ITODYS* laboratory at the Paris City University.
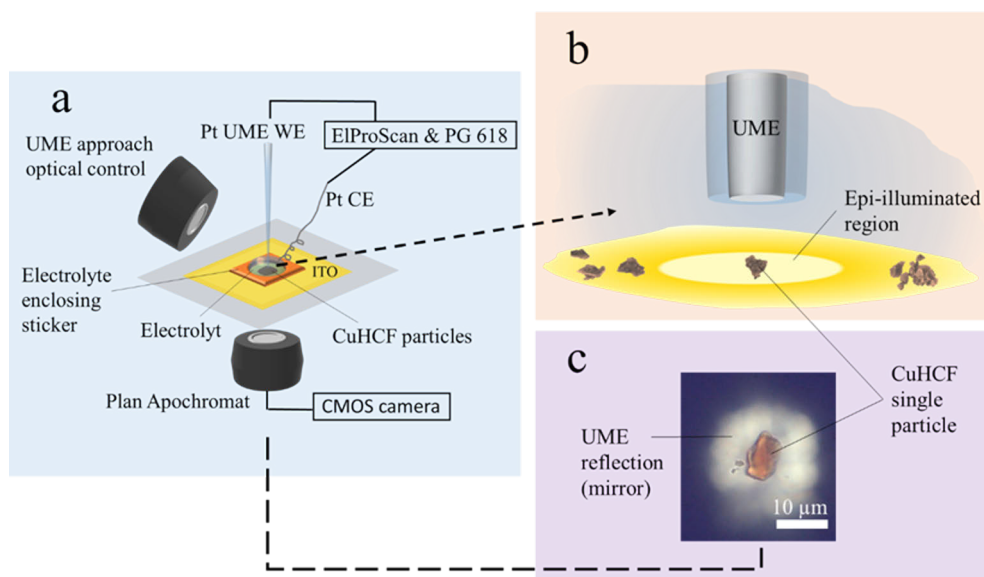

Figure 11. Optical paired SECM setup. **a)** macro-scale: CuHCF-drop casted ITO enclosed by redox electrolyte illuminated from the bottom through the objective lens (epi-illumination). **b)** micro-scale zoom in: the UME tip located 10µm away from the ITO surface to charge and discharge the particle via redox electrolyte. **c)** snapshot of CuHCF during charge. UME acts as a mirror enabling the abortion imaging of the particle.

5.2.3   Electron microscopy of CuHCF

The surface morphologies of CuHCF were studied by a Thermo Scientific Apreo S field emission scanning electron microscopy with an SETM detector. For SEM the CuHCF grinded powder was sprinkled on a carbon tape and imaging was operated with an accelerating voltage of 2kV and current of 13 pA (**Figure 12**). For STEM, a diluted dispersion of CuHCF in ethanol was drop-casted on a PELCO® TEM Grid with lacey carbon film. After drying, the imaging was operated with an accelerating voltage of 30 kV and current of 25 pA (**Figure 13**).
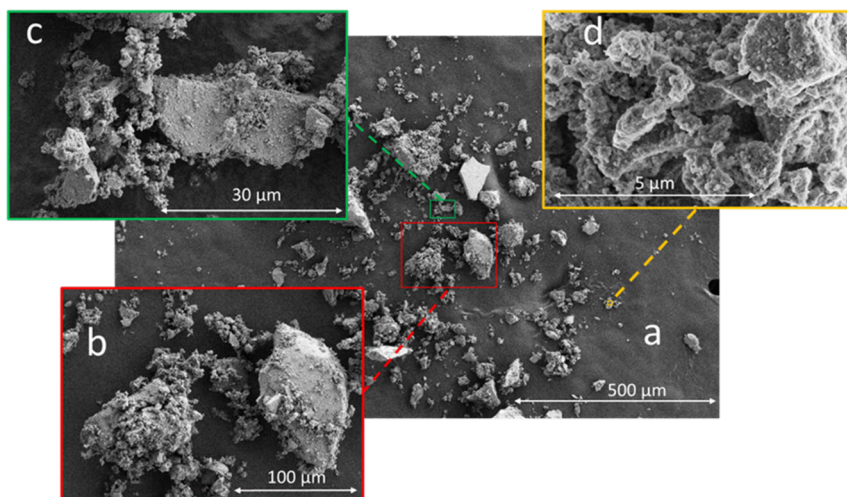

Figure 12. SEM image of CuHCF grinded powder on a carbon tape. **A**, **b**, and **c** show low-angle backscattered signals collected by Everhart–Thornley detector and **d** shows secondary electron signals collected by In-lens detector.
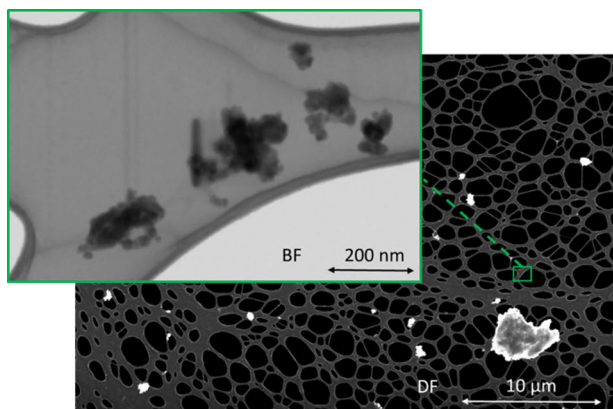

Figure 13. Dark field (DF) and bright field (BF) STEM images of CuHCF particles decorated on the lacey carbon support. Particles consist of agglomerates of nanocrystals.

5.2.4   X-ray diffraction of CuHCF

The powder diffractogram was obtained using Malvern Panalytical Empyrean diffractometer in θ/θ Bragg-Brentano configuration, with Cu K_α radiation and PIXcel3D detector in scanning line mode. The measurements were done with an angular step size of 0.026° with a 90s step time. Results are coherent with literature.[69]
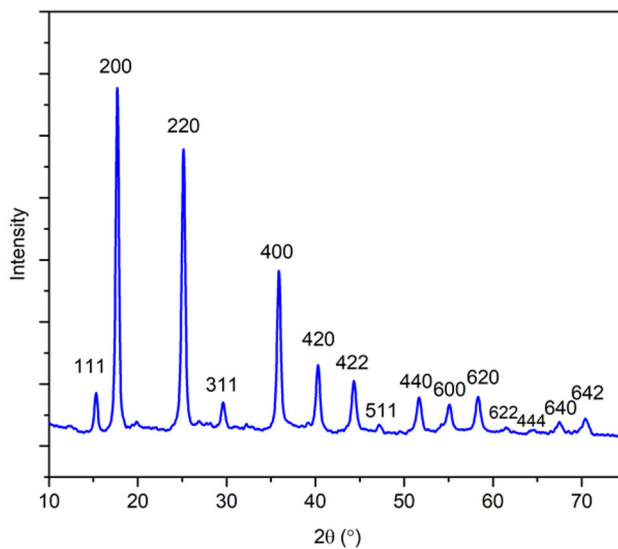

Figure 14. XRD pattern of synthesized CuHCF powder.

6 Results and Discussion

6.1 **Conversion:** Nafion induced oxygen absorption in electrocatalysts of PEM fuel cells

SECM is used to perturb the oxygen partition equilibrium over the porous electrocatalyst layers containing Nafion to study the presence of the absorbed oxygen within the electrocatalyst layers of PEM fuel cells. Samples with different combinations of presence of Nafion, carbon, and catalyst (20 wt-% Pt on carbon black) are included in this study. **Figure 15** shows all the sample substrates.
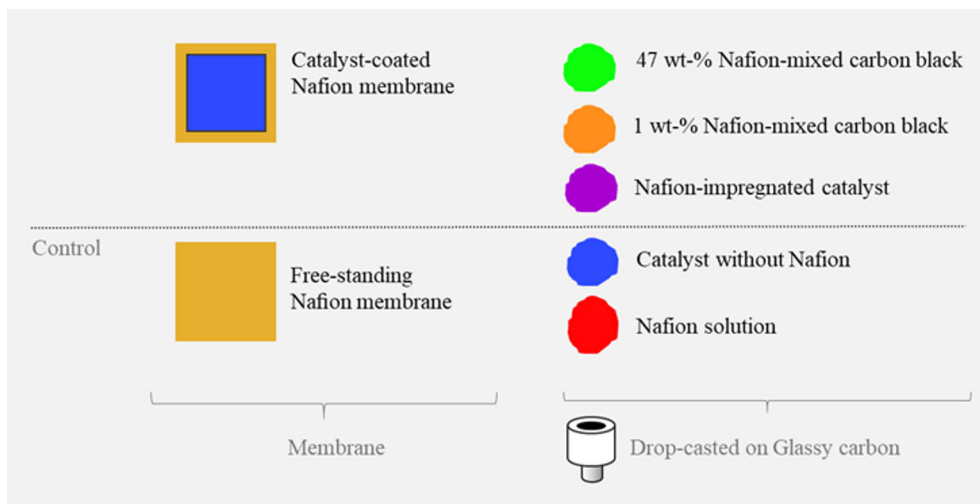

Figure 15. SECM sample substrates.[I]

As shown in **Figure 15**, in two samples the catalyst was in contact with Nafion: in one (yellow square with blue center), the catalyst ink was spray-coated on the Nafion membrane. In the other one (violet), the Nafion ionomer solution was drop-casted on a dried porous catalyst layer, which had previously been drop-casted on a GC. Further, Nafion solution (5 wt-%) was mixed with C65 carbon black and then drop-casted on the GC. One sample contained 1 wt-% of Nafion solution (orange) and the other sample contained 47 wt-% of Nafion solution (green), so the final

Nafion contents in the solution were 0.05 wt-% and 2.35 wt-%. In addition, control experiments were performed with a free-standing Nafion membrane (yellow square), a drop-casted Nafion ionomer (red) and a drop-casted catalyst ink (blue) on clean GC electrodes (refer to Experimental). Therefore, in total seven samples were selected for the SECM experiment.

During all the approach experiments, the SECM tip was biased for ORR. The potentials were selected based on CV curves in the bulk electrolyte prior to approach experiments. Bias potentials were located in the plateau window of the CVs shown in **Figure 16**.
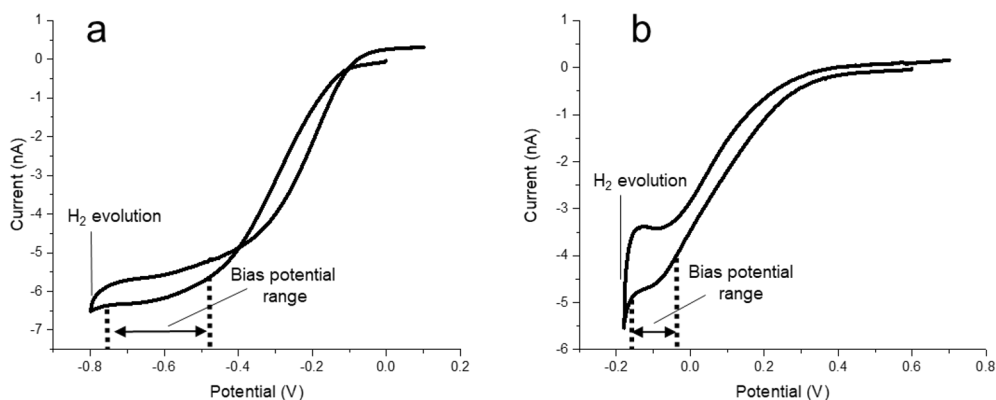

Figure 16. The bulk solution cyclic voltammetry **a)** for basic (KOH 0.1 M) and **b)** for acidic (H_2SO_4 0.5 M) media. The tip bias potential for approach curves and the substrate potential for oxygen depletion experiment in both media were selected from the potential window in which the plateau was observed.[I, SI]

Figure 17 and **Figure 18** show approach curves with normalized current and tip distance. The dashed lines represent the theoretical pure positive and negative feedback.
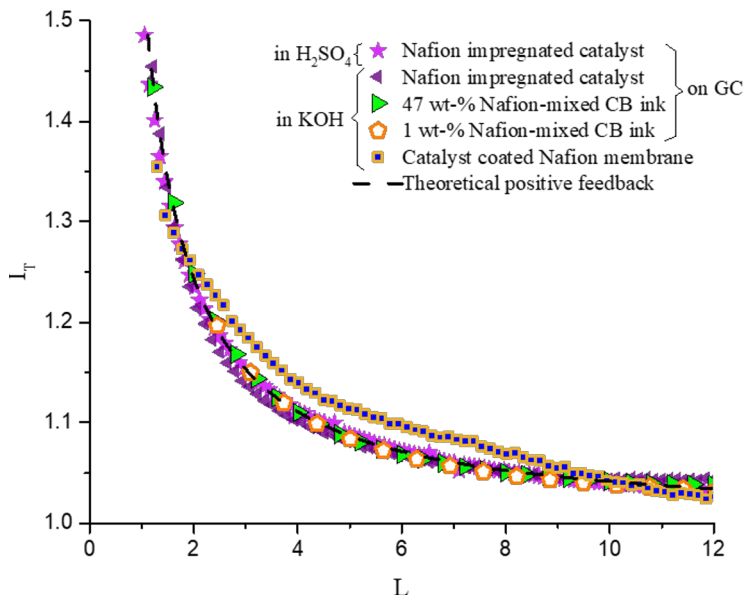
Figure 17. Current-distance response of the Pt tip approaching Nafion impregnated catalyst in H_2SO_4 (★) and in KOH (◀), and 47 wt-% Nafion-mixed (▶) and 1 wt-% Nafion-mixed (⬠) carbon black inks in KOH on GC, and catalyst coated Nafion membrane (■) in KOH. The dashed line represents the theoretical positive feedback.[I]

Both samples where Nafion and catalyst are in contact with each other, show positive feedback-like behavior. The catalyst coated Nafion membrane shows slight deviations from the theoretical positive feedback that might originate from two factors: first, the membrane is not fixed as in the other experiments with GC and it may not be completely horizontal when the tip approached the surface; second, microscopic topographic unevenness of the membrane might affect the solution interaction volume while the tip is a few microns away from the membrane.

In addition, as shown in **Figure 17**, in samples which does not contain any Pt, and only Nafion and carbon black are in contact with each other, a behavior similar to the positive feedback is observed.

Figure 18 shows approach curves for the samples with a negative feedback response.
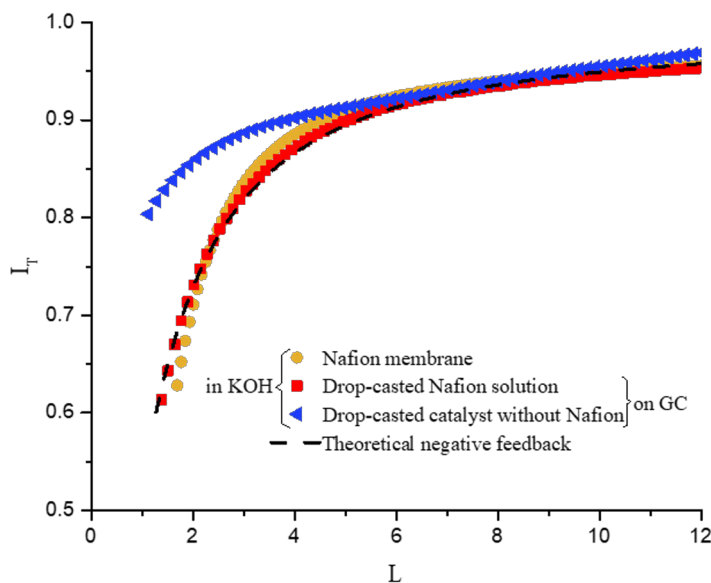
Figure 18. Current-distance response of the Pt tip in KOH electrolyte approaching a free-standing Nafion membrane (●), a drop-casted Nafion solution on GC (■), and a drop-casted catalyst without Nafion on GC (◄). The dashed line represents the theoretical negative feedback.[I]

Free standing Nafion membrane and drop casted Nafion on GC both exhibit an agreement to the pure negative feedback. The same behavior is observed on GC as the substrate without any pastes (results are not shown). The drop casted catalyst on GC shows a mixed response.

The current in the bulk is generated from reduction of the solvated oxygen at the SECM tip. Therefore, when the tip is approaching the substrate, any increase in the tip current indicates that a different source for oxygen is present; in other words an excess amount of oxygen is absorbed in the layer. In the situation where solvated oxygen is the only source and oxygen in the substrate is not significantly present, one would normally expect that approaching the tip to the substrate would result in negative feedback response.

Based on **Figure 18**, Nafion in both forms of membrane and drop casted solution on GC show close to pure negative feedback response. In addition, drop-casted carbon-supported catalyst without Nafion is showing a mixed response but with a current lower than the bulk. However, as observed in **Figure 17**, when Nafion (either in the form of drop-casted solution or membrane) and carbon supported catalyst or carbon back are present simultaneously, significant amount of additional oxygen is present in the substrate, according to observing the positive feedback response.

To investigate whether the oxygen present within the substrate is thermodynamically stable or if it is simply being trapped during the spray coating or drop-casting steps (thermodynamically unstable), the substrate was biased for ORR to deplete it from the oxygen. Using a bi-potentiostat, the tip was simultaneously biased with the same potential located a few microns away from the substrate. Currents at both the tip and the substrate reached zero confirming that the oxygen within the substrate and also the solvated oxygen in the vicinity of the substrate were depleted (reduced) during the experiment. Next, the substrate was disconnected and the tip was again biased for the ORR reaction. As a function of time, the current increased incrementally and finally reached higher than the bulk current confirming that the oxygen is again supplied from the substrate after being depleted previously. This validates that the oxygen is thermodynamically stable in the substrate and was recovered by partitioning from the bulk electrolyte into the substrate. The oxygen present in the catalyst layer is at equilibrium with the dissolved oxygen in the electrolyte.

As mentioned in 3.1.2, oxygen can be confined within the hydrophobic parts of the self-assembled Nafion ionomer on the graphitic surfaces of the catalyst's support, namely carbon black.[26,28] This confinement of oxygen in the substrate may be responsible for the observed positive feedback-type response. To further explore this phenomenon and determine whether platinum particles are essential for oxygen confinement, experiments were conducted using carbon black without any catalyst particles mixed with Nafion solution in two different ratios. As depicted in **Figure 17**, the Nafion-mixed carbon black inks without any Pt (▷ and ▢) exhibited a positive feedback response, indicating that the presence or absence of platinum particles in the substrate does not affect the oxygen confinement process. As a control experiment, the Nafion solution was also drop-casted onto a clean GC surface as shown in **Figure 18** (■). The approach experiment showed a negative feedback response, suggesting that no significant amount of oxygen is confined on the glassy surfaces of carbon.

6.1.1   Finite element simulations

Finite element simulations were performed to investigate the presence of oxygen within the drop-casted catalyst layer and how different parameters affect the SECM approach experiment. COMSOL Multiphysics details are available in the supporting information of **publication I**.

Generally, catalyst inks drop-casted on GC show porosities up to 0.6.[70] In the simulation carried out here, it is assumed that half of the void fraction is filled by electrolyte and the rest by gas phase. **Figure 19** depicts the situation where porosity is 0.6 and 50% of total volume of the voids are filled with the electrolyte and 50%

with the oxygen in gas phase. It should be noted that the real ratio of the electrolyte and gas phase is not known. Moreover, the gas phase volume should change when the oxygen is consumed and estimating this volume change requires more experimental data on distribution of the gas phase. X-ray micro-tomography could be utilized for better understanding the porous structure and distribution of the gas phase.
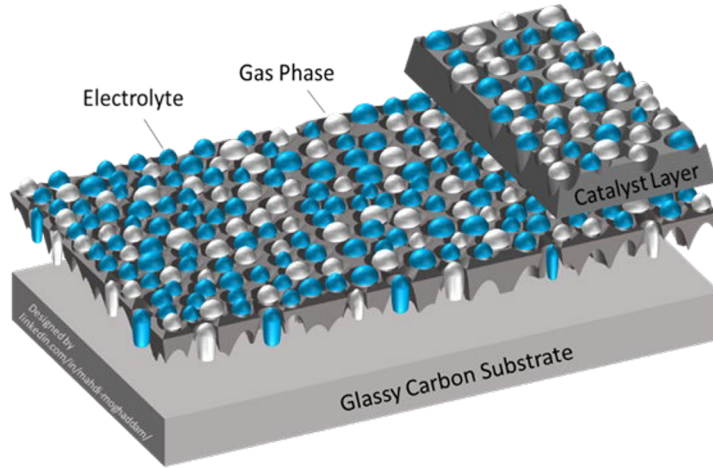

Figure 19. Drop casted catalyst layer on the GC. Porosity in the catalyst is 0.6, where half of the voids are filled with the electrolyte (blue), and the rest are filled with the gas phase (white). [I, SI]

The dissolved oxygen $O_2(aq)$ in the electrolyte over the catalyst layer is in equilibrium with the absorbed oxygen in the catalyst layer, $O_2(g)$:

$$O_2 \text{ (aq)} \rightleftharpoons O_2 \text{ (g)} \tag{21}$$

with the equilibrium constant or oxygen partition coefficient

$$K = \frac{c_{O_2(g)}}{c_{O_2(aq)}} = \frac{k_1}{k_{-1}} \tag{22}$$

where k_1 is the transfer rate of O_2 from the aqueous phase into the gas phase and k_{-1} is the transfer rate for the reverse reaction. By applying the ORR potential to the tip, the dissolved oxygen at the tip is reduced via reaction (23):

$$O_2(aq) + 2H_2O + 4e^- \rightarrow 4OH^-(aq) \tag{23}$$

If during the ORR the tip is a few microns away from the substrate, the oxygen partition equilibrium is perturbed over the porous catalyst layer as $O_2(aq)$ is being consumed. To retain the equilibrium, oxygen is supplied by transferring from the gaseous to aqueous phase indicating the effect of k_{-1} on the current collected at the tip. In addition, the oxygen diffusivity within the phase affects the system.

Figure 20 shows the simulated approach curves for different values of K, k_{-1}, and ε (porosity) of 0.6 and 0.8. The diffusion coefficient of oxygen in the aqueous phase ($1.93 \cdot 10^{-5}$ cm^2 s^{-1}) is utilized for the oxygen present in the catalyst layer. According to **Figure 20**, high enough partition coefficients and transfer rates show positive feedback responses. In addition, higher porosities shift the current towards positive feedback response. A high partition coefficient translates to a higher concentration of the excess oxygen within the catalyst compared to the dissolved oxygen in the electrolyte, $c_{O_2(g)}/c_{O_2(g)}$, while a high transfer rate translates to a higher interfacial area available for the reaction (21). As shown in **Figure 18**, the catalyst ink without Nafion (◄) shows a mixed response close to the negative feedback. As carbon black with high surface area is utilized as the catalyst support, high transfer rates are expected. Therefore, when compared to simulation results in **Figure 20**, mixed responses close to the negative feedback are due to the low partition coefficient. This indicates that no significant amount of oxygen is present in the catalyst layer in the absence of Nafion.
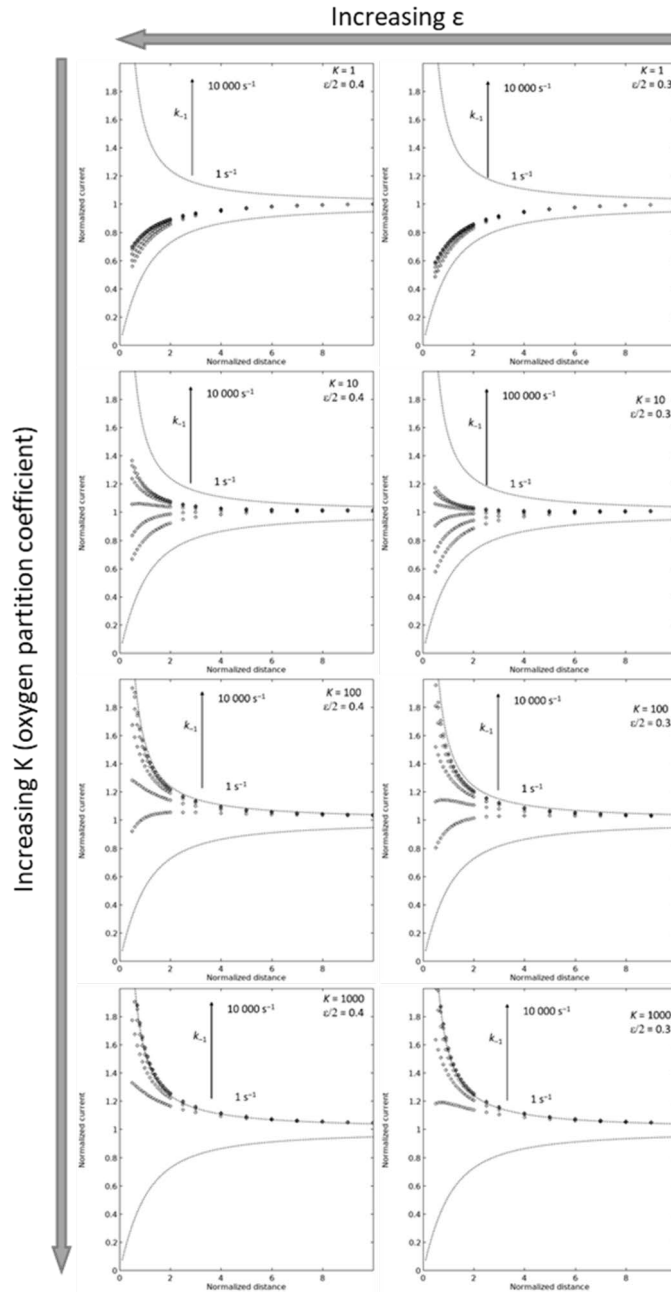
Figure 20. Simulated approach curves for electrode porosity ε of 0.6 and 0.8, partition coefficient K from 1 to 1000 and transfer rate from gas phase to aqueous phase from 1 to 10000 s^{-1} (steps of 1 order of magnitude). Diffusion coefficient of oxygen in the aqueous phase is utilized for excess oxygen absorbed in the catalyst layer. The volume fraction of the electrolyte phase is half the porosity of the electrode, and volume fraction of the gas phase is equal to the volume fraction of the electrolyte.[I, SI]

6.2   **Storage:** Charge transfer in flow batteries with solid boosters

Figure 21 shows an overview of a flow battery with solid boosters added to the tanks. In the negative side, the redox couple is introduced as red_1/ox_1 and the solid booster is introduced as red_2/ox_2. Most of the redox active solid materials show a poor electron conductivity and in practice, they need to be embedded in a conductive additive network such as carbon black using a binder. In **Figure 21** yellow solid boosters are embedded in the gray conductive carbon in the negative side.
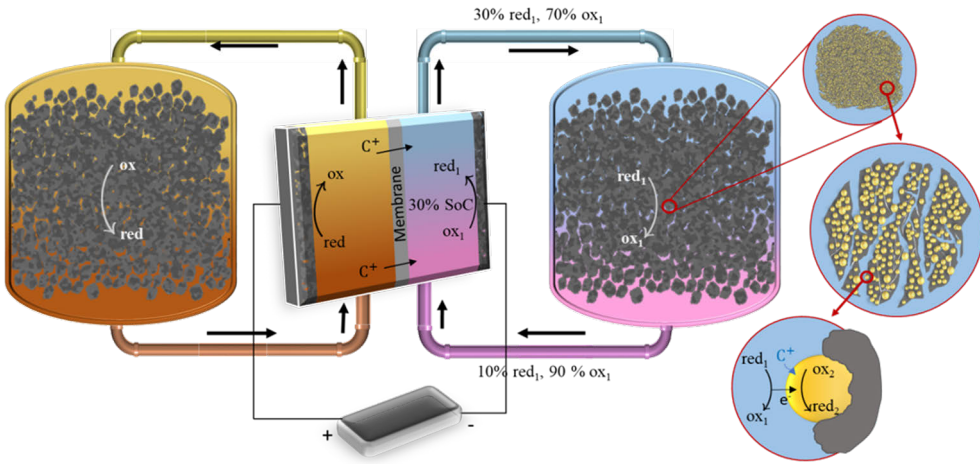

Figure 21. Overview of the solid boosted flow battery over multiple scales. Solid boosters are deposited in the tank as millimeter-sized porous beads, containing the redox active solid materials (ox_2/red_2 (yellow) for negative side), and conductive additive and binder (grey). In this example, on the negative side of the battery discharged electrolyte ox_1/red_1 is reduced in the cell from SoC of 10% to 30 %. Reduced dissolved species will then react in the tank to reduce the solid active material ox_2/red_2. This reaction is typically accompanied by intercalation of a cation C^+.[II]

In the negative side of the battery in the cell, ox_1 is reduced to red_1 via reaction (24) while for the sake of charge neutrality a cation, C^+, crosses the membrane from the positive side of the cell to the negative side of the cell:

$$ox_1 + e^- \xrightarrow{\text{cell}} red_1 \tag{24}$$

red_1 flows into the tank and on the surface of the redox solid it is oxidized back to ox_1 while a cation is intercalated into the solid to maintain the charge neutrality:

$$red_1 + ox_2 + C^+ \xrightarrow{\text{tank}} ox_1 + red_2 \qquad (25)$$
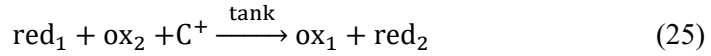
In this way, the redox solid is charged and regenerated ox_1 flows back to the cell and can once again be reduced. The charging continues until the equilibrium is reached between the redox electrolyte and the redox solid.

6.2.1 Non-equilibrium: charge storage and Fermi-level equilibration

Figure 22 depicts the solid's charging process in the negative side based on the Fermi level equilibration.
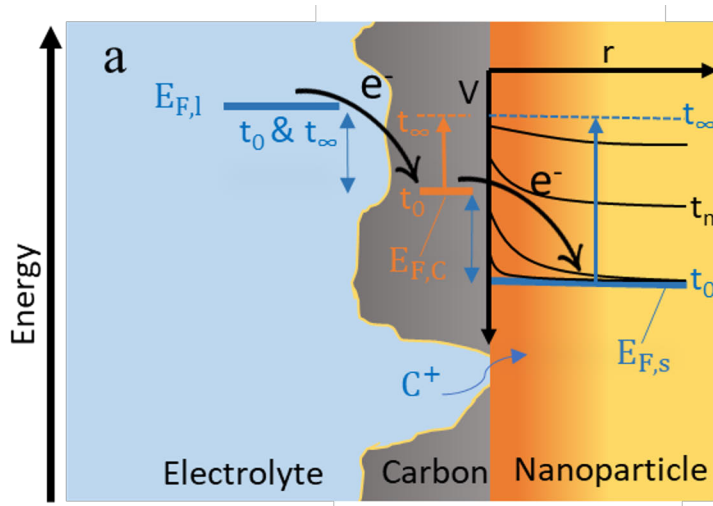

Figure 22. Solid booster's charging in the negative side of the flow battery based on Fermi level equilibration. Carbon shows a regulatory behavior. Energy scale has zero defined as electron at rest in vacuum, and increases from bottom to top. Potential *V* increases from top to bottom.[II]

We consider the situation where the cathodic current in reaction (24) is controlled to achieve a constant state of charge (SoC) of interest for the redox electrolyte (SoC_1). If the flow rate is adjusted so that fresh electrolyte is replacing all the reacted electrolyte, the Fermi level of the electrolyte, $E_{F,l}$, that is the potential dictated by the SoC_1, is considered constant. During charge, the Fermi level of the redox solid nanoparticle (that is in oxidized form), $E_{F,s}$, is located at a lower energy level compared to that of the electrolyte. Carbon shuttles the electrons from the

electrolyte to the solid and its Fermi level, $E_{F,C}$, locates between the $E_{F,l}$ and $E_{F,s}$, i.e. $E_{F,s} < E_{F,C} < E_{F,l}$.

At two ends of carbon, i.e. contact with the electrolyte and contact with the solid, two different reactions take place at the same time (**Figure 22**). One is electron transfer (ET) from the electrolyte to carbon (backward direction of reaction (24); $red_1 \rightarrow ox_1 + e^-$). With assuming small overpotentials linearized Butler-Volmer (BV) (refer to 2.2) defines the current as follows:

$$I_{ox} = A_{ox}i_{0,ox}f\eta_{ox} \tag{26}$$

At the other end, redox solid is charged through reaction (27)

$$ox_2 + e^- + C^+ \rightarrow red_2 \tag{27}$$

and its state of charge, SoC$_2$,increases gradually. With assuming the ET being the limiting factor for the reaction, and small overpotentials, the current according to linearized BV can be defined as follows:

$$I_{red} = A_{red}i_{0,red}f\eta_{red} \tag{28}$$

This situation satisfies the requirements for mixed potential theory[71] where two redox reactions, each engaging a different redox couple with different Fermi levels, take place simultaneously at two ends of carbon. At equilibrium half reactions at both ends proceed with the same rate for the sake of satisfying the zero net current on carbon ($I_{ox}=-I_{red}$). In order to maintain this equality, overpotentials η_{ox} and η_{red} will adjust accordingly. As oxidative current is positive, $\eta_{ox} > 0$ and similarly $\eta_{red}< 0$. As carbon is highly conducting, virtually no potential drop is assumed within carbon, and the Fermi level of the carbon will change by the corresponding change in the capacitive surface charge. The position of $E_{F,C}$ relative to $E_{F,s}$ and $E_{F,l}$ defines the overpotentials at two ends of carbon since the overpotential is the driving force for the electron to move from one Fermi level to another (**Figure 22**). If $A_{red}i_{0,red} \neq A_{ox}i_{0,ox}$, $E_{F,C}$ locates closer to the Fermi level of the side with larger $A \times i_0$ so that the reaction at the other end experiences a larger overpotential. In this way the product of $A \times i_0 \times \eta$ would be equal and both reactions run with the same rate ($I_{ox}=I_{red}$). In principle, if the exchange current densities are different ($i_{0,ox}\neq i_{0,red}$), one might tailor the areas in order to ensure comparable driving forces $\eta_{ox} \approx \eta_{red}$ (i.e., $A_{ox}/A_{red} \approx i_{0,red}/i_{0,ox}$) in order to avoid excessive electrochemical losses for one of the half-reactions.

This regulatory behavior of carbon stays in effect throughout the chemical charge process where SoC$_2$ elevates. As charging of the solid requires diffusion of C$^+$ into

the solid, the increase in $E_{F,s}$ follows a diffusion controlled profile (**Figure 22**). As time passes, both $E_{F,s}$ and $E_{F,C}$ shift to higher levels. The change in the Fermi level of the carbon will require change in the capacitive surface charge, so the assumption of the net zero current is not completely accurate, but this deviation is considered small. At equilibrium (t_∞), $E_{F,s} \approx E_{F,C} \approx E_{F,l}$. In real case, sufficiently high flow rates to keep the Fermi level of the redox electrolyte constant would be impractical. Instead, concentration ratio of the reduced and oxidized species would change close to the interface due the reaction (21), and some mass transfer limitations would also arise.

As mentioned earlier, SoC_1 governs the charging process of the redox solid and consequently increase of SoC_2. In addition, inherent redox potentials of the redox couple and the redox solid affect the charging process. In the following, with thermodynamics treatments, the relationship between states of charge of the electrolyte and the solid with their redox potentials is illustrated.

6.2.2   Equilibrium: thermodynamics and total state of charge

Corresponding Nernstian relationships for reaction (24) and (27) are shown in equations (29) and (30) respectively:

$$E_1 = E_1^0 + \frac{RT}{F} \ln \left(\frac{a_{\mathrm{ox}_1}}{a_{\mathrm{red}_1}} \right) \tag{29}$$

$$E_2 = E_2^0 + \frac{RT}{F} \ln \left(\frac{a_{\mathrm{ox}_2} a_{C^+}}{a_{\mathrm{red}_2}} \right) \tag{30}$$

where E_1^0 and E_2^0 are the standard redox potentials of the electrolyte and the booster, respectively.

The overall reaction happening in the tank (reaction (25)) is the sum of reaction (27) and the backward direction of reaction (24). The potential expression of reaction (25) is shown in equation (31):

$$\begin{aligned} E_{\mathrm{overall}} &= E_2 - E_1 \\ &= E_2^0 - E_1^0 + \frac{RT}{F} \ln \left(\frac{a_{\mathrm{ox}_2} a_{C^+}}{a_{\mathrm{red}_2}} \right) - \frac{RT}{F} \ln \left(\frac{a_{\mathrm{ox}_1}}{a_{\mathrm{red}_1}} \right) \\ &= E_2^0 - E_1^0 + \frac{RT}{F} \ln \left(\frac{a_{\mathrm{ox}_2} a_{\mathrm{red}_1} a_{C^+}}{a_{\mathrm{ox}_1} a_{\mathrm{red}_2}} \right) \end{aligned} \tag{31}$$

With assuming the activity of C^+ as unity and the linear variation of the states of charge with the activities of the redox species, SoC_1 and SoC_2 can be defined respectively as follows:

$$SoC_1 = a_{ox_1} = 1 - a_{red_1} \tag{32}$$

$$SoC_2 = a_{ox_2} = 1 - a_{red_2} \tag{33}$$

With substitution of equations (32) and (33) into equation (31) at equilibrium ($E_{overall} = 0$), accessible state of charge of the redox solid, SoC_2, is obtained:

$$SOC_2 = \frac{SOC_1 e^{\frac{F(E_1^0 - E_2^0)}{RT}}}{(1 - SOC_1) + SOC_1 e^{\frac{F(E_1^0 - E_2^0)}{RT}}} \tag{34}$$

Figure 23 shows the total accessible state of charge of the solid vs the potential mismatch between the solid booster and the electrolyte based on equation (34).
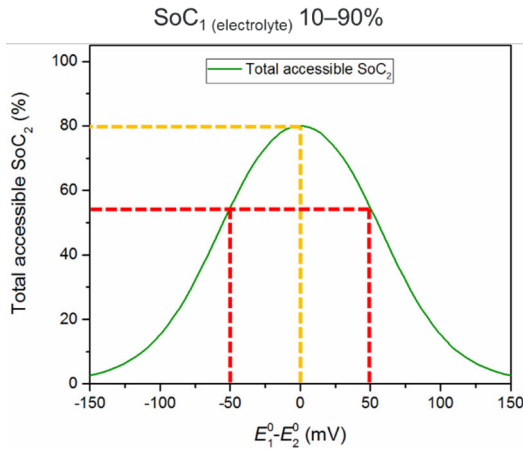

Figure 23. The total accessible SoC of the solid vs the potential mismatch between the solid booster and the electrolyte.[II]

With assuming the electrolyte being cycled between 10 and 90 percent SoC, the total accessible state of charge of the electrolyte, SoC_1, is 80 percent. With matching redox potentials of the electrolyte and the solid, i.e. $E_1^0 - E_2^0 = 0$, based on equation (34) $SoC_1 = SoC_2$ and 80% of the solid booster's state of charge can be accessed (yellow dashed line). However, even seemingly small mismatches in the redox potentials can largely decrease the accessible state of charge of the solid. As shown

in **Figure 23**, 50 mV of difference in redox potentials (red dashed lines) can decrease the accessible SoC from 80% to around 55%.

As redox potentials of many solid materials deviate from equation (29), real measured redox potential of copper hexacyanoferrate (CuHCF) is taken as an example for solid booster in the positive side of a SB-FB. **Figure 24** shows potential as a function of state of charge for CuHCF as the solid booster and different Nernstian redox couples. The potential curve for CuHCF is obtained from Wessells et al.'s work[69] while potential curves of different redox couples follow the Nernst equation with different standard redox potentials, considering activity coefficient ratio of 1 for reduced and oxidized species.
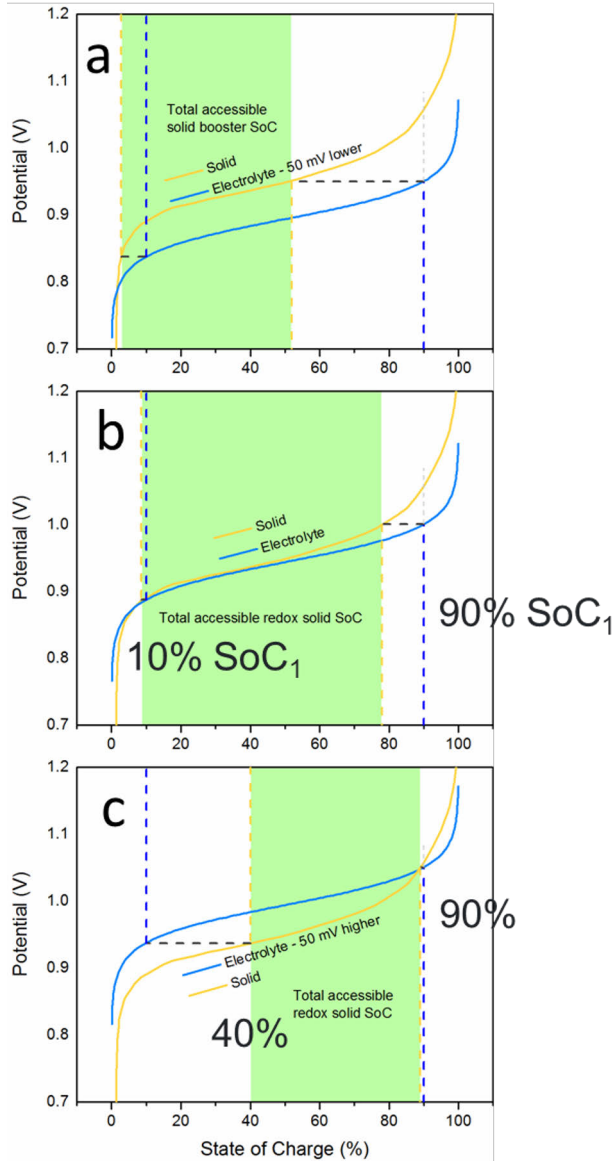
Figure 24. Accessible SoC of solid booster as a function of electrolyte potential. **a)** E_1^0 is 50 mV lower than E_2^0. **b)** $E_1^0 = E_2^0$. **c)** E_1^0 is 50 mV higher than E_2^0.[II]

In figure **Figure 24**, the area between blue dashed lines depict the accessible state of charge of the electrolyte, i.e. 90-10=80%. The applied potential for charging or discharging the solid depends on the state of charge of the electrolyte and the state of charge of solid will approach equilibrium with the electrolyte. The area in green color between the yellow dashed lines, show the total accessible state of charge of the solid. In case of matching redox potentials, charging the electrolyte up to 90%

state of charge will equilibrate with the solid at about 78% state of charge. During discharge, with reaching 10% state of charge of the electrolyte, the obtained potential is able to discharge the solid until 8% of the state of charge. Therefore, the total accessible state of charge of the solid would be 78-8=70%. However, in cases where redox potential of the solid differs 50 mV from the electrolyte, similar calculations show that the total accessible state of charge of the solid decreases drastically, i.e. the green area is decreased in **Figure 24**. Thus, potential disparity of the solid and the electrolyte greatly limit the total accessible state of charge of the solid.

6.2.3 Operational requirement: booster's available surface area is critical

The following section will discuss technical requirements of operation of the solid boosted system based on kinetics and thermodynamics of electron transfer reactions in the cell and in the tank.

Based on BV equation, currents of reaction (24) and reaction (25) can be written as equations (35) and (36) respectively if overpotentials are sufficiently large:

$$I_{cell} = -A_{cell}i_{0cell}e^{(\alpha-1)f\eta_{cell}} \tag{35}$$

$$I_{tank} = A_{tank}i_{0tank}e^{\alpha f\eta_{tank}} \tag{36}$$

Note that current in the cell is reductive, i.e. I_{cell} and $\eta_{cell} < 0$, while I_{tank} and $\eta_{tank} > 0$. Let us assume that the conversion current of the redox couple in the cell is equal to the conversion current in the tank:

$$-I_{cell} = I_{tank} \Rightarrow A_{cell}i_0e^{(\alpha-1)f\eta_{cell}} = A_{tank}i_0e^{\alpha f\eta_{tank}} \tag{37}$$

With rearranging and assuming α as 0.5, overpotential in the tank is related to overpotential in the cell and to the fraction of available surface areas and exchange currents in the cell and in the tank:

$$\eta_{tank} = |\eta_{cell}| + \frac{ln\left(\frac{A_{cell}i_{0,cell}}{A_{tank}i_{0,tank}}\right)}{0.5\,f} \tag{38}$$

As an experimental example the case of phosphonate group–substituted viologen | ferrocyanide flow battery in the reference [72] is taken for demonstrating the concept (**Figure 25**).
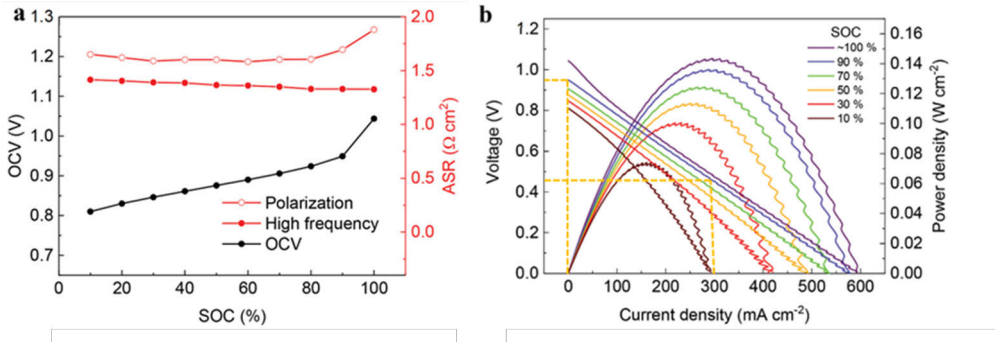
Figure 25. A real case flow battery performance. Reproduced (adapted) with permission from WILEY.[72] **a)** OCV, high frequency and polarization ASR versus SoC. **b)** cell voltage and power density during discharge at various SoC.

As shown in **Figure 25**, at current density of 300 mA/cm² the SoC can change for a maximum of 10%. With assuming the inflow electrolyte of 90% SoC into the cell, the outflow would be 80% meaning that the Nernst potential of the electrolyte will change by 21 mV. 21 mV is the thermodynamically available over potential (the driving force) provided by the electrolyte, for driving reaction (25) in the tank. If the overpotential in the tank, η_{tank}, is smaller than the available overpotential, redox conversion of the electrolyte in the tank takes place according to reaction (25). According to equation (38), for obtaining the same conversion rates in the tank and in the cell, the fraction of available surface areas in the tank and in the cell, A_{tank}/A_{cell}, should be optimized based on the exchange current densities and the overpotential in the cell.

Let's proceed with the same example system of **Figure 25**. In equation (38) $|\eta_{cell}|$ could be estimated with experiments. Making the estimation that voltage drop in polarization curve (V_{OCV}-V_i) is sum of iR-drop and of two equal overpotentials (for cathode and anode reaction), the calculated overpotential for one electrode in the cell is:

$$|\eta_{cell}| = (V_{OCV} - V_i - iR_{el})/2 \qquad (39)$$

With the same assumption of inflow electrolyte of 90% SoC and current density of 300 mA/cm² the high frequency resistance (R_{el}) of the cell is 1.3 Ω cm² (**Figure 25**). With locating the current (yellow dashed lines), V_{OCV} is 0.95 V and V_i is 0.45. Therefore $|\eta_{cell}|$ is calcluted as follows:

$$|\eta_{cell}| = \frac{0.95 - 0.45 - 300 \times 1.3}{2} = 0.055 \text{ V} \qquad (40)$$

Figure 26 shows η_{tank} vs. A_{tank}/A_{cell} for different ratios of exchange current densities based on equation (38). The dashed line shows the thermodynamically available over potential of 21 mV. In case of equal exchange current densities the active surface area in the tank should be at least three times larger than that of in the cell so that $\eta_{tank} < 21$ mV. The larger the exchange current density in the cell, the more surface area should be available in the tank. If $i_{0cell}/i_{0tank} = 10$ the active area of the tank should be thirty times larger than the area of the electrodes. Negative values for η_{tank} in **Figure 26** indicates that equation (38) is not valid for small overpotentials in the tank (not smaller than *ca.* 60 mV as shown in **Figure 2**).
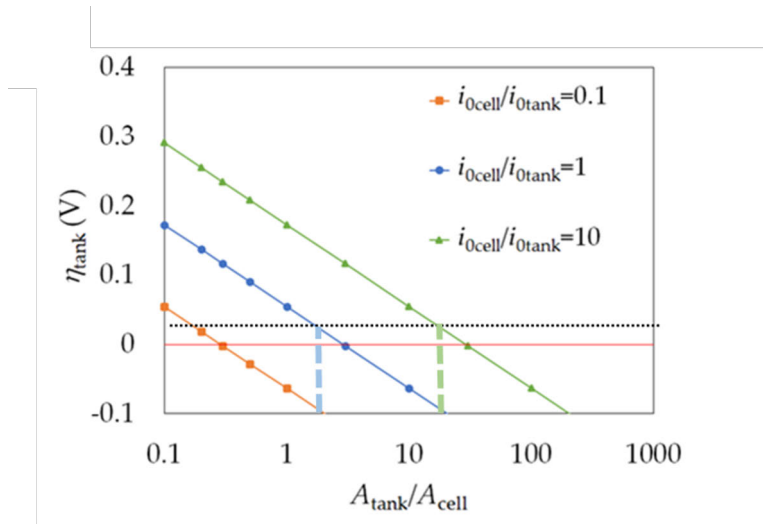

Figure 26. Dependence of the overpotential in the tank (η_{tank}) on the ratio of A_{tank}/A_{cell} for three different exchange current ratios based on equation (38). The overpotential in the electrode ($|\eta_{cell}|$) is 0.055 V. Dashed line marks the 21 mV of overpotential available from the 10% SoC change.[II]

In case of small overpotentials in the tank the Butler-Volmer equation can be linearized for the tank:

$$-I_{cell} = I_{tank} \Rightarrow A_{cell}i_0e^{(\alpha-1)f\eta_{cell}} = A_{tank}i_0f\eta_{tank} \qquad (41)$$

and with rearranging and assuming α as 0.5, overpotential in the tank is calculated as follows:

$$\eta_{tank} = \frac{A_{cell}i_{0,cell}e^{0.5f|\eta_{cell}|}}{A_{tank}i_{0,tank}f} \qquad (42)$$

Figure 27 shows η_{tank} *vs.* A_{tank}/A_{cell} for different ratios of exchange current densities based on equation (42). Now with increasing the fraction of A_{tank}/A_{cell} the η_{tank} is converging to zero instead of showing false negative values. More accurate calculations requires numerical simulations.
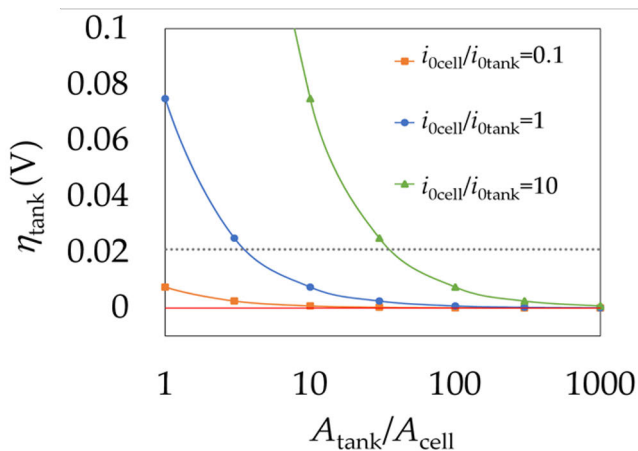

Figure 27. Dependence of the overpotential in the tank (η_{tank}) on the ratio of A_{tank}/A_{cell} for three different exchange current ratios based on equation (42). The overpotential in the electrode ($|\eta_{cell}|$) is 0.055 V. Dashed line marks the 21 mV of overpotential available from the 10% SoC change.[II]

6.2.4 Probing the local paths of charge transfer operando in booster-microparticles

In the following an *operando* high-resolution imaging methodology for the intricate coupled electron-ion transfer between the solid booster and the redox electrolyte is discussed in the case of the conversion of a single micrometric secondary particle of copper hexacyanoferrate (CuHCF) consisting of agglomerates of primary nanosized particles.

Using an UME in SI-SECM mode (refer to 4.1.1), provides a powerful platform for *operando* study of such conversion. This approach enables the tracking of charge storage/extraction in the redox solid at the microscale.

Meanwhile, optical microscopy techniques provide exceptional spatial, temporal, and throughput resolution, granting insights into the electrochemistry of energy storage materials at micro-[73–75] and nano-[76–81] scales. For instance, Wang *et al.* evaluated the K^+ diffusion dynamics within single PB nanoparticles.[76–78] Meanwhile, Merryweather *et al.*[73,74] showed how optical microscopy allows imaging *operando* the Li^+ insertion front lines within single micrometric battery particles during their oxidation/reduction.

Here, to gain insights into the local sub-micron conversion, the study combines SECM with optical microscopy. In this novel approach, depicted in **Figure 28**, UME serves as an optical mirror, allowing to investigate local changes in absorption and to probe the coupled electron transfer and K^+ (de)intercalation from/into single micrometric porous CuHCF particles. This combination allows for the investigation of charge transfer considering not only the microstructure but also the assembly of primary particles building the microparticle along with the intrinsic porosity of such assembly. In addition, it further reveals different charge transfer behaviors of capacitor-like or bulk-like conversions. It proposes a new methodology for better understanding of charge transfer not only for solid boosters but also for other secondary particles of active battery material.

6.2.4.1   Principals of opto-electrochemical microscopy

Figure 28 illustrates the electrochemical reaction environment (zoomed of **Figure 11**). CuHCF particles are drop-casted from a diluted water suspension on an ITO substrate and dried in room temperature. The redox electrolyte, 5mM TEMPTMPA redox couple (R/O^+) dissolved in 1M potassium nitrate, surrounds the CuHCF-drop casted ITO making a two-electrode enclosed system with Pt UME as the working electrode (WE) and a Pt wire as the counter electrode (CE).
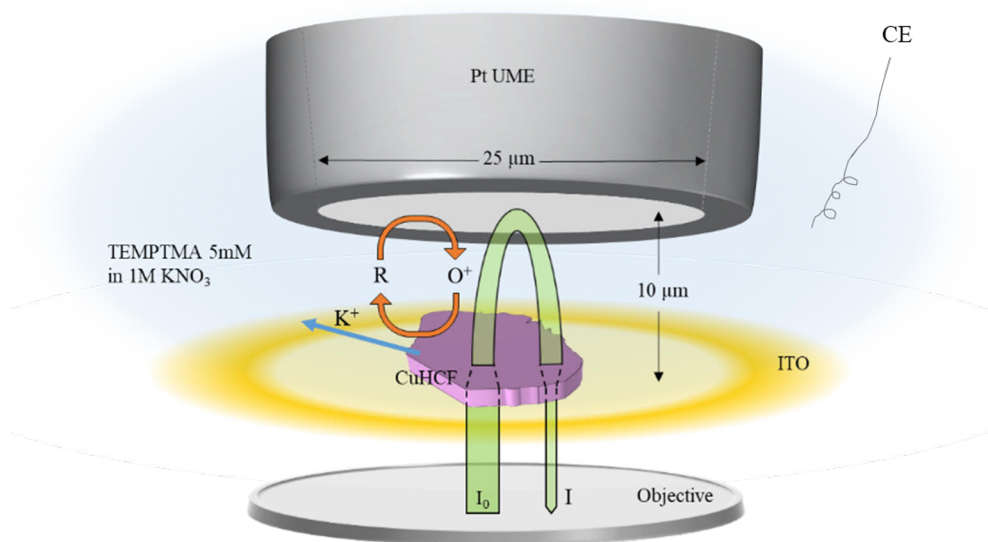

Figure 28. Optical paired SECM environment. CuHCF-drop-casted ITO is enclosed by TEMTPMA electrolyte and is illuminated from the bottom. Pt UME is 10 μm away from the ITO substrate (for bigger scale refer to **Figure 11**).

Both pristine CuHCF and TEMPTMA are in reduced form. CuHCF is chemically charged and discharged through TEMPTMA redox couple. When Pt UME is biased higher than $E_{redox,\ TEMPTMA}$ (+0.91 V $vs.$ SHE), TEMPTMA is oxidized at the tip ($R \rightarrow O^+$), the equilibrium around the tip is perturbed and a concentration gradient is generated. Produced O^+ species diffuse in the electrolyte towards the CuHCF particle a few microns underneath the tip. Meanwhile, R species diffuse reversely from the vicinity of the particle to the tip. Therefore, the equilibrium around the particle's surface is also perturbed. To compensate the R deficiency around the particle, electrons are supplied from the particle to be exchanged with O^+ species and regenerate R. For the sake of charge neutrality, Fe^{II} oxidizes to Fe^{III} within the particle and K^+ ions deintercalate from tetrahedral sites into the electrolyte. Reaction (43) (CuHCF discharge) takes place at the particle's surface:

$$K_2Cu[Fe^{II}(CN)_6] + O^+ \rightleftharpoons KCu[Fe^{III}(CN)_6] + \theta + R + K^+ \tag{43}$$
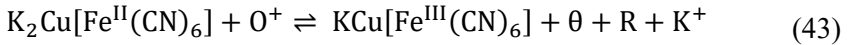
where O^+ is the oxidized TEMPTMA, θ represents the potassium ion site in CuHCF, and R is the reduced TEMPTMA. For CuHCF charging, reaction (43) proceeds reversely.

The setup is illuminated from the bottom through the objective lens and the optical signal is recorded during chronoamperometry (CA) and cyclic voltammetry (CV) measurements. The potential profiles are shown in **Figure 30**, **top**. To obtain the absorbance variation of CuHCF particle during its conversion, background (electrolyte) effect should be excluded from the optical signals. To do so, firstly two control regions (50×50 pixel) are selected; one outside the particle but within the UME reflection region and the other one within the particle shown in **Figure 29 a**. Secondly, averages of variation of intensity are extracted from these two regions as $I_0(t)$ and $I(t)$ and are shown for each color channel in **Figure 29 b** and **c** respectively (note that I in this section only refers to light intensity). The variation during the cyclic voltammetry measurement is shown at the top and during the chronoamperometry measurement is shown at the bottom. Lastly, the average absorbance variation of the CuHCF particle (control region within the particle) is calculated as following:
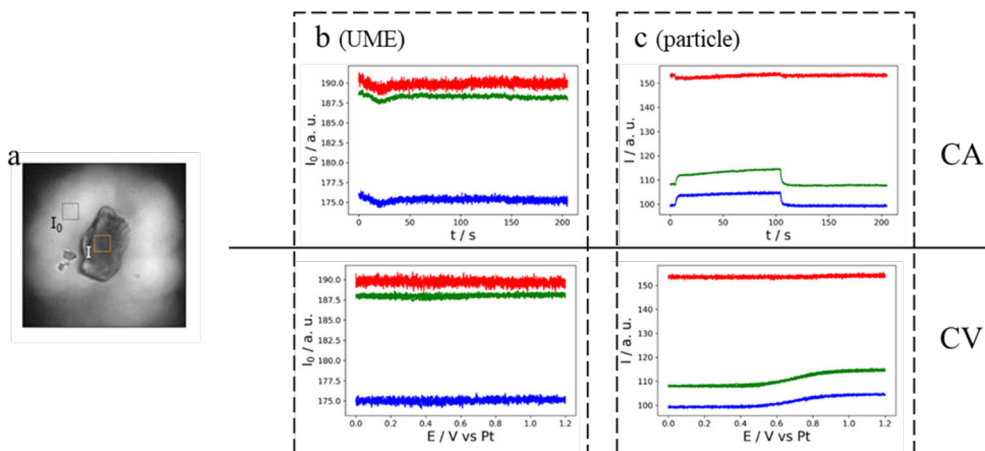
$$A(t) = \log\left(\frac{I_0(t)}{I(t)}\right) \tag{44}$$

Figure 29. Average intensity variations. **a)** two 50x50 pixel (2.75x2.75 μm^2) control regions over which the intensity variation is recorded; one outside the particle (and within the UME reflection area) and one within the particle. **b)** average intensity variation of the selected region within the UME reflection during CA **(top)** and CV **(bottom)**. **c)** average intensity variation of the selected region within the particle during CA **(top)** and CV **(bottom)**. Results are obtained for CuHCF particle in 5 mM TEMPTMA + 1 M KNO$_3$. The red, green, and blue lines represent the intensity variations in the red, green, and blue color channel, respectively.[III, SI]

6.2.4.2   Proportionality of absorbance variation and exchanged charge

For the green channel, according to equation (44), the average absorbance variations within the control region inside the particle (A_g) for CV and CA measurements are shown in **Figure 30 a, bottom** and **b, bottom**, respectively. Corresponding electrochemical measurements are shown at the top.
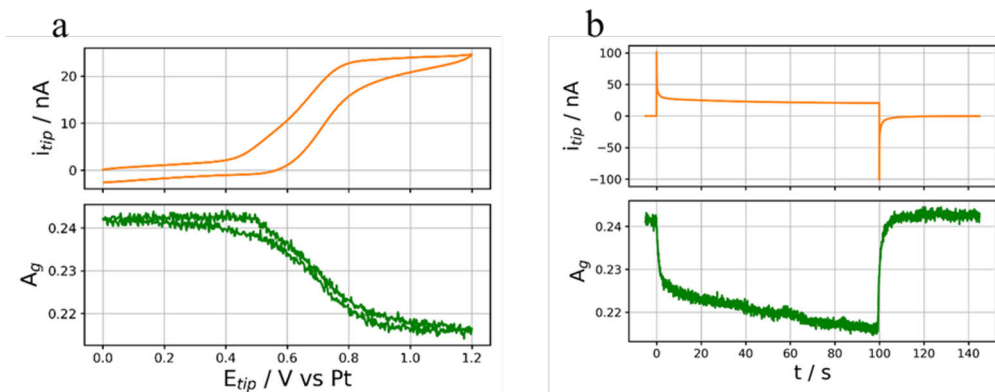

Figure 30. Comparison between global electrochemical response **(top)** and average absorbance variation **(bottom)** in **a)** CV and **b)** CA measurements.[III]

CA experiments are used as the basis for studying the dynamics of particle conversion. As shown in **Figure 30 b**, at first, according to the observed plateau current in CV (**Figure 30 a**), the tip is biased for 100 s at 1.1 V *vs.* Pt to oxidize the redox electrolyte. During the first step, produced O^+ is delivered to the particle to oxidize it. The drastic absorption variation occurs during short times (0-5s) and thereafter during longer times (>5s) the absorption varies with a much less pronounced manner. In the second step, the tip potential is changed back to 0 V to reduce the particle.

The collected current at the tip during the CA is a global electrochemical response from the particle while the optical response, i.e. the absorption variation, can be read locally with one pixel being the accuracy. For the absorbance variation to be electrochemically perceptible, its global response should be correlated with the charge associated with conversion of the CuHCF. **Figure 31**, **top**, shows a zoom-in of the first 5 seconds of the CA, i.e. short-term dynamics, shown in **Figure 30 b, top** along with a background current (dashed line) overlaid to the original graph. The background current is obtained from a control CA measurement taken over an area empty of particles. Current values obtained over the particle are higher than the values obtained with no particle under the tip but both eventually converge to a similar steady state current. The additional current over the particle is caused by the regeneration of R species at the particle's surface as it is being oxidized. To calculate the exchanged charge during the particle conversion, currents from control CA experiment over the CuHCF-devoid region is subtracted from CA over the particle and the resulted current is integrated over time for the first 5 seconds of the experiment. The resulted value, Q_M (nC), is an estimation of the global charge exchanged during the conversion of the particle.
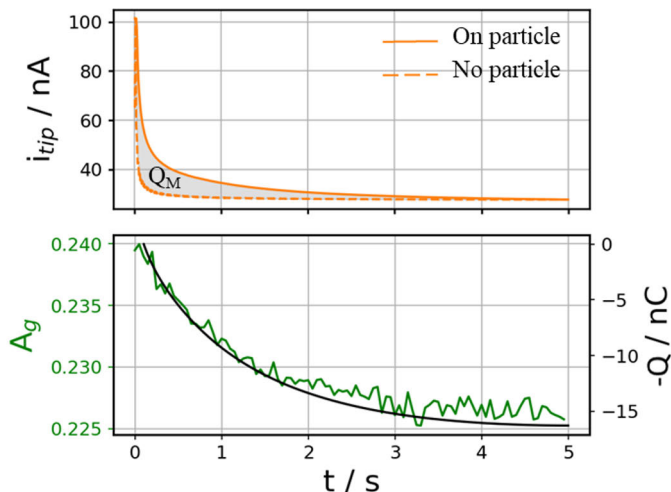
Figure 31. Tip current responses over particle (solid line) and over a particle-devoid region (dashed line) with Q_M as the global exchanged charge **(top)**. Comparison between the global electrochemical charge profile (estimated based on Q_M) and the average absorbance variation **(bottom)**.[III]

The charging of the particle as a function of time can be fitted with an exponential function:

$$Q(t) = Q_M(1 - e^{-k_{app}t}) \tag{45}$$

where $k_{app} = 1/\tau_{app}$ is the apparent conversion rate and τ_{app} is the characteristic conversion time. The global absorption variation, $A(t)$, can now be compared to the global electrochemical charge profile, $Q(t)$. $A(t)$ can be defined with a similar exponential function:

$$A(t) = A_{bg} + \Delta A \, e^{-k_{app}t} \tag{46}$$

where A_{bg} is the background absorbance before the oxidation potential pulse and ΔA is the total absorbance variation compared to A_{bg}. Note that A_{bg} is defined for each pixel individually.

With similar characteristic conversion rates, using equations (45) and (46), the global electrochemical response is correlated to the global absorption variation:

$$\frac{Q(t)}{Q_M} = 1 - \frac{A(t) - A_{bg}}{\Delta A} \tag{47}$$

Based on equation (47), **Figure 31, bottom** compares the absorption variation, $A(t)$, with the electrochemical charge, $Q(t)$, as a function of time.

6.2.4.3 Sub-particle imaging: local maps of exchanged charge and conversion rates

The proportionality of $Q(t)$ and $A(t)$ is used as a rationale for local response in each pixel of the image; with having the optical signal of each pixel at any given time, it is possible to calculate the corresponding exchanged charge. Furthermore, based on equation (46) , k_{app} is obtained for each pixel.

The maps of local maximum exchanged charge (q_M mC cm^{-2}) and apparent rate for particle's oxidation are shown in **Figure 32 b** and **c**, respectively, and **a** shows the raw image of the particle before starting the CA. The k_{app} is evaluated by considering either the first 5 s (k_{app}^{5s}) or 15 s (k_{app}^{15s}) of the optical signal variations after the potential pulse. These images characterize respectively the short-term or long-term conversion of the oxidation step previously explained according to **Figure 30 b, bottom**.

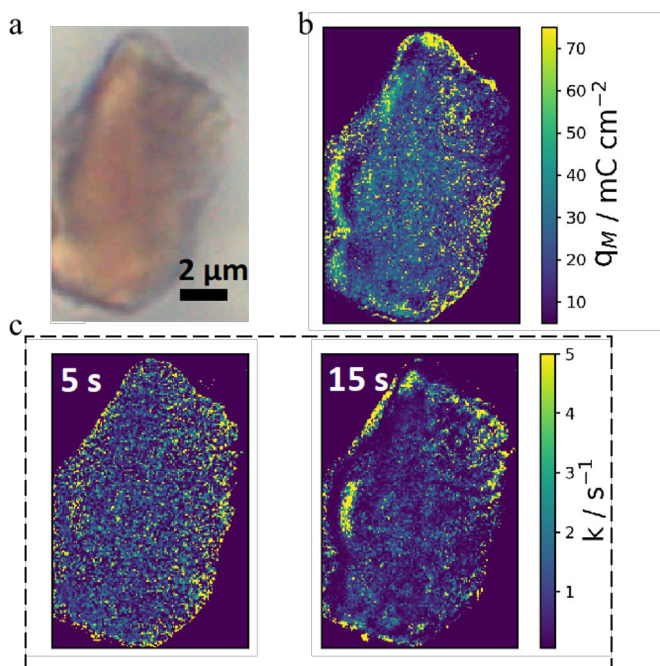**Figure 32.** Imaging the local oxidation of a CuHCF single microparticle. **a)** raw image before the potential pulse. **b)** local maximum exchanged charge. **c)** local conversion rates at short-term (5 s) and long-term (15s) regimes.[III, SI]

According to **Figure 32 c** (and also **Figure 33 c** and **d),** during short times the distribution of conversion rate is quite homogenous throughout the particle while at longer times a strong heterogeneity is observed in different regions of the particle. Interestingly, this heterogeneity is related to the local material loading and local exchanged charge within the particle. To better observe this correlation, **Figure 33** provides a zoomed-in view (5x7.5 μm^2) of the upper-right part of the particle (ca. $1/3^{rd}$ of the whole particle) in **Figure 32**.

Figure 33 a presents a map of the background absorption of the green channel before the oxidation potential pulse: regions with higher absorption ($a_{g,bg}$), contain greater amounts of CuHCF. It means either that the particle is thicker or that primary particles are more densely packed within these regions. The red contours in highlight regions with high material loading, while the white contours highlight regions with low material loading.

Figure 33 b depicts the local maximum exchanged charge. It is expected that the higher the loading, the higher the amount of exchanged charge. This trend is generally observed across the particle. However, despite this general trend, this correlation does not hold uniformly in all regions. For instance, regions #1 and #2 marked by white contours exhibit relatively low loading but high exchanged charge. This suggests the presence of regions with higher porosity or smaller nanocrystals, enabling deeper bulk conversion.

Figure 33 c presents short-term local oxidation conversion rate and **d** presents the ratio of long-term and short-term rates. Contrary to the observed homogenous rate distribution at short times that makes it difficult to distinguish between regions of high (red contours) and low (white contours) material loading (**Figure 33 c**), during long-term conversion some regions show rates of up to 100 times slower than the short-term rates (note the logarithmic scale of **Figure 33 d**), highlighting the heterogeneous distribution of the conversion rate.
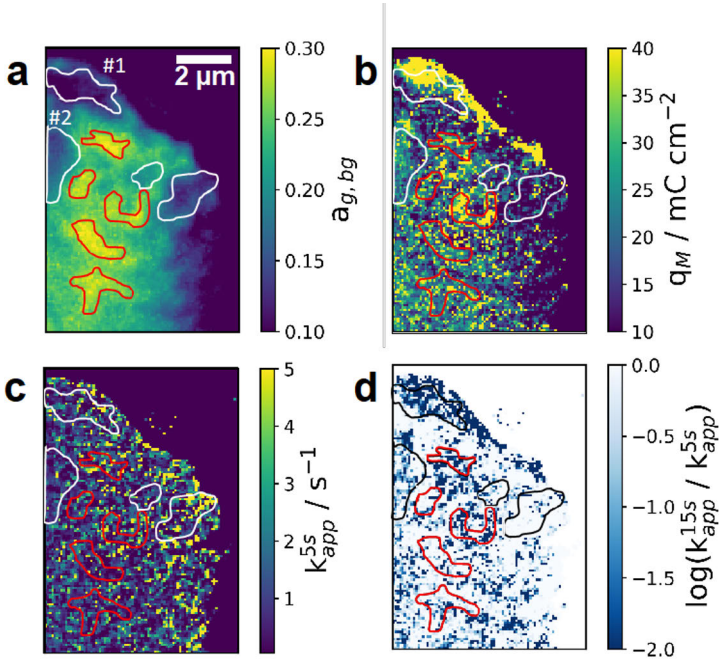
Figure 33. Imaging the local oxidation. **a)** local absorbance variations (local loading). **b)** local exchanged charge. **c)** local short-term oxidation rate. **d)** ratio of the short-term (k_{app}^{5s}) and long-term (k_{app}^{15s}) oxidation rates.[III]

This observation aligns with the heterogeneous maps of material loading or maximum exchanged charge presented in **Figure 33 a,** and **b**. The higher the material loading, the higher exchanged charge, and the slower the conversion rates (and the darker the pixels in **Figure 33 d**; compare red contours). However, noteworthy that this correlation again does not hold uniformly across all regions. In regions #1 and #2 for instance, the local exchanged charge (q_M) appears to influence the conversion rates more strongly than material loading (a_{bg}). Within these specific regions, areas characterized by a higher electrochemical charge but with low loading exhibit slower and deeper oxidation revealing regions with higher porosity or smaller nanocrystals. These optical maps thus unveil mechanistically relevant behaviors, potentially linked to the local nanostructure or porosity of the particle.

6.2.4.4 Surface and bulk conversion of porous structure rationalized with simulation

The homogenous and faster rates at short times suggest an initial surface-confined conversion (like the recent observation for Prussian blue single-nanocrystal)[78]. After the initial stage, CuHCF undergoes a deeper bulk diffusion as observed in 6.2.4.3

through the slower rates at longer times. This approach, considering a surface conversion followed by a bulk conversion, is rationalized with COMSOL simulations in the following.

As observed in post mortem electron microscopy images of the studied particle in **Figure 34 a** (and of the synthesized CuHCF powder in **Figure 12** and **Figure 13**), the particle is a secondary particle consisting of assemblies of primary particles. This structure confers porosity inside the particle and favors the surface-confined conversion, which is why porous PBAs are utilized as supercapacitors.[66] The porosity of the CuHCF microparticles was confirmed by measuring N_2 adsorption/desorption isotherms (BET analysis). The analysis suggests mesoporosity located between the primary particles with an average pore diameter of around 9 nm and a specific surface area of $S_S \approx 10^2 \text{ m}^2 \text{ g}^{-1}$ (detailed calculation in section S6, SI of the Publication III).
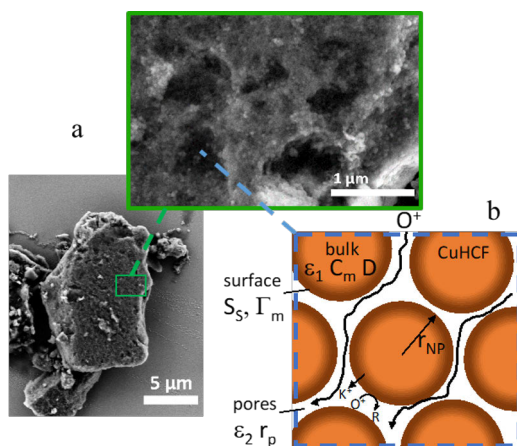

Figure 34. Microparticle structure. **a)** post mortem SEM images of the studied particle. **b)** schematic description of the COMSOL model.[III]

Figure 34 b presents the schematic description of the model accounting for transport of O^+ species (introduced in **Figure 28**) in a porous network: the microparticle is made of spherical primary particles (radius r_{NP}) in a cubic close-packed network separated by voids with the porosity volume of ε_2 (solid volume fraction is $\varepsilon_1 = 1 - \varepsilon_2$) and pore radius of r_p. The nanoparticle conversion takes into account a surface conversion with surface concentration of Γ_m, and a diffusive conversion with bulk concentration of C_m. D is the diffusion coefficient for potassium inside the solid.

Simulation results of the potentiostatic oxidation of the secondary particle are presented in **Figure 35**. **Figure 35 a** demonstrates the impact of the K^+ diffusion

coefficient inside the CuHCF (D) on the particle's average conversion dynamics considering either the conversion of the surface+bulk (plain lines) or only the bulk conversion (dashed lines) of the primary particle of 30 nm radius. Higher D values make surface conversion negligible (compare plain and dashed lines for $D = 10^{-12}$ cm^2 s^{-1}), while lower D values make surface conversion predominant (compare plain and dashed lines for $D = 10^{-15}$ cm^2 s^{-1}).
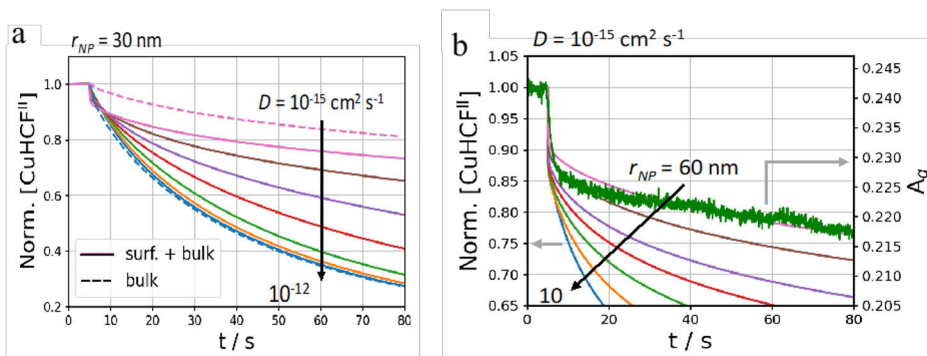

Figure 35. Simulation results for potentiostatic oxidation of the secondary particle. **a)** effect of diffusion coefficient inside the primary particle. **b)** effect of primary particle's radius compared with experimental absorbance variation.[III]

Figure 35 b explores the influence of the size of the primary particles on the conversion dynamics, showing that larger radii produce a faster initial surface conversion, followed, at longer times, by a slower bulk-like conversion. In addition, the experimental absorbance variation (previously discussed in **Figure 30**) is also displayed along the simulated curves. It matches well with the simulation considering a porous assembly of primary particles of 50 nm radius and a diffusion coefficient of the order of 10^{-15} cm^2 s^{-1}, within the range of some reported values for PBAs.[82]

The simulations effectively replicate the experimental observations of the initial rapid conversion followed by a slower one at longer times. The initial rapid conversion ($t < 5$ s) is attributed to the surface conversion of the nanosized primary particles, while the slower, deeper conversion at longer times corresponds to the bulk conversion of primary particles.

Conclusion and outlook

In this thesis in the context of energy conversion materials, electrocatalyst layers containing carbon black and Nafion were investigated with SECM feedback mode. It was shown that Nafion in either forms of membrane or film formed by drop-casting, cannot confine the oxygen in its structure. Similarly, the drop-casted catalyst (20 wt-% Pt on carbon black) on glassy carbon without the presence of Nafion is unable to confine significant amounts of oxygen. In contrast, it was shown when Nafion and the catalyst coexist in the layer, oxygen is detected within the electrocatalyst's structure. It is suggested that the oxygen is confined within the hydrophobic part of the self-assembled ionomer on graphitic surfaces of the catalyst's support, maintaining an equilibrium with the solvated oxygen in the electrolyte. In addition it was observed that the presence or absence of Pt particles does not affect the Nafion self-assembly and the consequent oxygen confinement.

In the context of energy storage materials, charge transfer in solid active (booster) particles in flow batteries was studied. First, the charge storage principals were conceptualized with fundamental kinetics and Fermi-level equilibration. Moreover, with thermodynamical treatment the total accessible state of charge of the solid particle was formulated. The smaller the redox potential difference between the solid and the redox electrolyte, the greater the stored charge in the solid. Even small mismatches of 50 mV can result in drastic decrease in total accessible state of charge. In addition, it was shown that booster's available surface area is a critical technical requirement for operation of solid boosted flow batteries. The surface area for electrochemical reaction on the booster affects the required overpotential. With crossing a critical portion of the area in the tank (booster's) over the area in the cell (A_{tank}/A_{cell}) the thermodynamically available overpotential will be more than the required overpotential and therefore even small overpotentials due to changes in the SoC of the electrolyte are adequate to drive the reactions at reasonable rates on the booster's surface.

Second, the intricate conversion dynamics of secondary CuHCF microparticles composed of nanoscale primary particles was investigated as solid boosters. The SECM and high-spatial resolution optical microscopy were combined to shed light on the conversion behavior both at the global and local scales. On one hand, SECM

allowed to target individual particles and monitor their electrochemical conversion at the global scale. On the other hand, in a novel approach the SECM UME acted as an optical mirror making absorbance measurement possible with optical microscopy and providing a rationale for the conversion of the optical signal into a state-of-charge and conversion rate. This combination allowed imaging the conversion at the sub-micrometer level revealing a homogeneous surface conversion of nanocrystallites of parimary particles at short time followed by their slower and more heterogeneous bulk conversion. The heterogeneous regions are likely originating from locally different porosities or different nanocrystal size distribution. COMSOL simulations further confirmed the different surface and bulk conversion regimes.

Finally, potential future studies that can be built on this thesis are discussed in the following. If a fuel cell is supplied with air, it may potentially reach a mass transfer limitation for oxygen. Under such circumstances, any excess absorbed oxygen would subsequently be converted into water. In the case of gas evolution reactions, oxygen partitions into the catalyst layer, mitigating oversaturation in the liquid phase and consequently retarding the formation of bubbles.[I] Conducting simulations that account for these phenomena is essential to assess the practical implications of oxygen absorption within the catalyst layer on fuel cell and electrolyzer performance. Additionally, performing experimental comparisons involving various catalyst supports, such as functionalized carbon, nanotubes, graphene, as well as non-carbon alternatives like TiO_2, SiC, and other oxide-based materials, could yield valuable insights.[I] Other open questions are: how does the hydrophobicity of the catalyst layer contribute to the absorbed oxygen? Also, will other gases like hydrogen show the same behavior? While SECM proves to be a valuable tool for assessing these effects, there is a need for enhanced quantification of the experiments and a more comprehensive understanding of the electrocatalyst layer's structure such as porosity.

The novel proposed *operando* imaging of secondary booster particles[III] offers significant potential to advance the understanding of charge transfer mechanisms in nanostructured materials. Exploiting further this screening methodology should provide a rationale for the design of new porous materials not only utilized as solid boosters but also as active materials involving intercalation/deintercalation processes in other energy storage systems. To investigate more the solid boosted system, it would be interesting to image a configuration that further includes conductive additives and binders in contact with the solid active particles to know how they can practically affect the charge transfer dynamics. Moreover, a transparent microfluidic flow cell containing stationary solid booster particles in the flow chamber could be integrated in a flow battery setup to include the transport phenomena in the study. The integrated part can be placed in an optical microscope to investigate the charge transfer dynamics operando during charge/discharge of the battery.

Acknowledgements

First, I would like to extend my gratitude to my supervisor, Professor Pekka Peljo. His down-to-earth attitude helped me to be able to ask for his advice anytime I needed it. His magnificent support for attending numerous conferences and learning environments provided me with the opportunity to grow my network, meet and collaborate with brilliant researchers, and thrive in research. His calmness and kindness provided me with a peaceful and stress-free state of mind throughout the PhD journey. Next, I thank Professor Kati Miettunen for giving me the courage to apply and succeed in acquiring external funding. Additionally, I am grateful to Professor Milica Todorović for being there whenever I needed her professional advice at work. I also express my gratitude, for proofreading my dissertation draft, to Dr. Ulriika Mattinen, whose personality inspire me. I would also like to thank Professor Vipul Sharma for his support during the final stages of writing the dissertation.

I am greatly thankful to Dr. Frédéric Kanoufi for his kind hospitality during my stay at ITODYS in Paris. I never forget how diligently he supervised the experiments and how kindly and patiently he discussed and explained the science. Next, I would like to thank Dr. Louis Godeffroy that without his great contribution **Publication III**

could not have turned out this great. His expertise in data analysis is spectacular. In addition, I would like to thank all my co-authors at ITODYS: Dr. Jean-Marc Noël, Dr. Jean-François Lemineur, Dr. Nikolaos Kostopoulos, and Dr. Jean Yves Piquemal. Thank you for the great hospitality, the great company during lunches, and the lovely goodbye cake. I warmly thank my co-author Dr. Jerzy J. Jasielec for his contribution and insights in my published and unpublished research. Collaborating with him is a pleasure. I am also grateful to all my co-authors in **Publication II**: Dr. Silver Sepp, Dr. Cedrik Wiberg, Professor Antonio Bertei, and Dr. José Alexis Rucci.

I also extend my heartfelt gratitude to Professor Alireza Babaei whose continuous support during all these years was a source of inspiration.

I thank all the past and present members of the Battery Materials and Technologies group for the great time we shared. In addition, I am grateful to everyone in the Materials Engineering unit for the enjoyable Fikas we had every Friday together. Special thanks go to Ermei Mäkilä and Sari Granroth for their generous assistance and the fruitful discussions on XRD, XPS, and Electron Microscopy measurements. My thanks also go to Mikael for his genuine willingness to help with any problem at work, to Emilia for her patience in speaking Finnish with me, to Maryam for the delightful anonymous sweets she often brought to work and her enjoyable company during the breaks, and to Alicja for her kind company and support during challenging times at work.

I warmly thank my dear friends who brought happiness and warmth to my life, both at work and beyond, throughout the PhD journey. Moein in Naples, Mahroo, Roozbeh, Kuldeep, Fatemeh, Mohammad, Wouter, and Pegah in Helsinki, Pauline, Maryam, Keivan, and Mohammad in Paris, Saeid in Metz, Saeedeh in Vienna, Nasrin, Armin, Melina, Sanaz, Elmira, Polychronis, Nina, Jan, Claudia, Tato, Nani, Gabriel, Aya, Asmaa, and friends in Aava music group in Turku.

I warmly thank my dear family in Iran for their amazing emotional support during all the years of being far away from my first home. I thank Sima for being there unconditionally in all the ups and downs in life for as long as I can remember. I thank maman and baba, Ensiyeh and Fereydoon, for their incomparable and consistent support. For teaching me how to selflessly love, how to sacrifice for gain, how to (try to) be kind, and how to endure the dark until the light emerges. And I thank my dearest Justus for his precious presence and the utmost happiness he brings along, as tender as a breeze in June, wafting over lilacs.

Turku, 28.11.2023
Mahdi Moghaddam

List of References

1. Bard, A. J. & Faulkner, L. R. *Electrochemical Methods: Fundamentals and Applications*. (John Wiley & Sons, Inc., 2001).
2. Girault, H. H. (Hubert H.). *Analytical and physical electrochemistry*. (EPFL, 2004).
3. Sun, M. H. *et al.* Applications of hierarchically structured porous materials from energy storage and conversion, catalysis, photocatalysis, adsorption, separation, and sensing to biomedicine. *Chem Soc Rev* **45**, 3479–3563 (2016).
4. Liu, C., Li, F., Lai-Peng, M. & Cheng, H. M. Advanced materials for energy storage. *Advanced Materials* vol. 22 Preprint at https://doi.org/10.1002/adma.200903328 (2010).
5. Aricò, A. S., Bruce, P., Scrosati, B., Tarascon, J.-M. & Schalkwijk, W. Van. *Nanostructured materials for advanced energy conversion and storage devices*. www.nature.com/naturematerials (2005).
6. Li, W., Liu, J. & Zhao, D. Mesoporous materials for energy conversion and storage devices. *Nat Rev Mater* **1**, 16023 (2016).
7. Brandon, N. P., Skinner, S. & Steele, B. C. H. Recent Advances in Materials for Fuel Cells. *Annual Review of Materials Research* vol. 33 183–213 Preprint at https://doi.org/10.1146/annurev.matsci.33.022802.094122 (2003).
8. Steele, B. C. H. & Heinzel, A. *Materials for fuel-cell technologies*. www.nature.com (2001).
9. Wang, Y., Ruiz Diaz, D. F., Chen, K. S., Wang, Z. & Adroher, X. C. Materials, technological status, and fundamentals of PEM fuel cells – A review. *Materials Today* vol. 32 178–203 Preprint at https://doi.org/10.1016/j.mattod.2019.06.005 (2020).
10. Gür, T. M. Review of electrical energy storage technologies, materials and systems: Challenges and prospects for large-scale grid storage. *Energy and Environmental Science* vol. 11 2696–2767 Preprint at https://doi.org/10.1039/c8ee01419a (2018).
11. Peighambardoust, S. J., Rowshanzamir, S. & Amjadi, M. Review of the proton exchange membranes for fuel cell applications. in *International Journal of Hydrogen Energy* vol. 35 9349–9384 (2010).
12. Walkowiak-Kulikowska, J., Wolska, J. & Koroniak, H. Polymers application in proton exchange membranes for fuel cells (PEMFCs). *Physical Sciences Reviews* vol. 2 Preprint at https://doi.org/10.1515/psr-2017-0018 (2017).
13. Zhang, J. *PEM Fuel Cell Electrocatalysts and Catalyst Layers Fundamentals and Applications*. *PEM Fuel Cell Electrocatalysts and Catalyst Layers* (Springer, 2008).
14. Cindrella, L. *et al.* Gas diffusion layer for proton exchange membrane fuel cells-A review. *Journal of Power Sources* vol. 194 146–160 Preprint at https://doi.org/10.1016/j.jpowsour.2009.04.005 (2009).
15. Mehta, V. & Cooper, J. S. Review and analysis of PEM fuel cell design and manufacturing. *J Power Sources* **114**, 32–53 (2002).
16. Mansor, N. B. *Doctoral thesis: Development of Catalysts and Catalyst Supports for Polymer Electrolyte Fuel Cells*. (2014).

17. Ma, S., Chen, Q., Jøgensen, F. H., Stein, P. C. & Skou, E. M. 19F NMR studies of Nafion™ ionomer adsorption on PEMFC catalysts and supporting carbons. *Solid State Ion* **178**, 1568–1575 (2007).

18. Rastrick, I. D. Modified Gas Diffusion Electrode for Proton Exchange Membrane Fuel Cells. in *Proceedings of the Symposium on Diaphragms, Separators, and Ion-Exchange Membranes* 172–178 (1986).

19. Srinivasan, S., Ticianelli, E. A., Derouin, C. R. & Redondo, A. Advances in solid polymer electrolyte fuel cell technology with low platinum loading electrodes. *J Power Sources* **22**, 359–375 (1988).

20. Szajdzinska-Pietek, E., Schlick, S. & Plonka, A. Self-Assembling of Perfluorinated Polymeric Surfactants in Water. Electron Spin Resonance Spectra of Nitroxide Spin Probes in Nafion Solutions and Swollen Membranes. *Langmuir* **10**, 1101–1109 (1994).

21. Jiang, S., Xia, K. Q. & Xu, G. Effect of additives on self-assembling behavior of Nafion in aqueous media. *Macromolecules* **34**, 7783–7788 (2001).

22. Jia, W., Tang, B. & Wu, P. Novel Slightly Reduced Graphene Oxide Based Proton Exchange Membrane with Constructed Long-Range Ionic Nanochannels via Self-Assembling of Nafion. *ACS Appl Mater Interfaces* **9**, 22620–22627 (2017).

23. Modestino, M. A. *et al.* Self-assembly and transport limitations in confined nafion films. *Macromolecules* **46**, 867–873 (2013).

24. Chen, Y. *et al.* Electrochemical study of temperature and Nafion effects on interface property for oxygen reduction reaction. *Ionics (Kiel)* **24**, 3905–3914 (2018).

25. Antolini, E., Giorgi, L., Pozio, A. & Passalacqua, E. Influence of Nafion loading in the catalyst layer of gas-diffusion electrodes for PEFC. *J Power Sources* **77**, 136–142 (1999).

26. Chlistunoff, J. & Sansiñena, J. M. Nafion Induced Surface Confinement of Oxygen in Carbon-Supported Oxygen Reduction Catalysts. *Journal of Physical Chemistry C* **120**, 28038–28048 (2016).

27. Chlistunoff, J. & Sansiñena, J. M. On the use of Nafion® in electrochemical studies of carbon supported oxygen reduction catalysts in aqueous media. *Journal of Electroanalytical Chemistry* **780**, 134–146 (2016).

28. Chlistunoff, J. RRDE and voltammetric study of ORR on pyrolyzed fe/polyaniline catalyst. on the origins of variable tafel slopes. *Journal of Physical Chemistry C* **115**, 6496–6507 (2011).

29. Zhang, H., Li, X. & Zhang, J. *Redox flow batteries: Fundamentals and applications. Redox Flow Batteries: Fundamentals and Applications* (CRC Press, 2017). doi:10.1201/9781315152684.

30. Roth, C., Noack, J. & Skyllas-Kazacos, M. *Flow Batteries: From Fundamentals to Applications.* (Wiley-VCH, 2022).

31. Winsberg, J., Hagemann, T., Janoschka, T., Hager, M. D. & Schubert, U. S. Redox-Flow Batteries: From Metals to Organic Redox-Active Materials. *Angewandte Chemie - International Edition* **56**, 686–711 (2017).

32. Noack, J., Roznyatovskaya, N., Herr, T. & Fischer, P. The Chemistry of Redox-Flow Batteries. *Angewandte Chemie - International Edition* **54**, 9776–9809 (2015).

33. Sánchez-Díez, E. *et al.* Redox flow batteries: Status and perspective towards sustainable stationary energy storage. *J Power Sources* **481**, 228804 (2021).

34. Vesborg, P. C. K. & Jaramillo, T. F. Addressing the terawatt challenge: Scalability in the supply of chemical elements for renewable energy. *RSC Advances* vol. 2 7933–7947 Preprint at https://doi.org/10.1039/c2ra20839c (2012).

35. Zanzola, E. *et al.* Solid electrochemical energy storage for aqueous redox flow batteries: The case of copper hexacyanoferrate. *Electrochim Acta* **321**, 134704 (2019).

36. Vivo-Vilches, J. F. *et al.* LiFePO4-ferri/ferrocyanide redox targeting aqueous posolyte: Set-up, efficiency and kinetics. *J Power Sources* **488**, 229387 (2021).

37. Yan, R. *et al.* Determining Li+-Coupled Redox Targeting Reaction Kinetics of Battery Materials with Scanning Electrochemical Microscopy. *Journal of Physical Chemistry Letters* **9**, 491–496 (2018).

38. Jennings, J. R., Huang, Q. & Wang, Q. Kinetics of LixFePO4 Lithiation/Delithiation by Ferrocene-Based Redox Mediators: An Electrochemical Approach. *Journal of Physical Chemistry C* **119**, 17522–17528 (2015).

39. Zhou, M. *et al.* Nernstian-Potential-Driven Redox-Targeting Reactions of Battery Materials. *Chem* **3**, 1036–1049 (2017).

40. Gupta, D. & Koenig, G. M. Analysis of Chemical and Electrochemical Lithiation/Delithiation of a Lithium-Ion Cathode Material. *J Electrochem Soc* **167**, 020537 (2020).

41. Wang, Q., Zakeeruddin, S. M., Wang, D., Exnar, I. & Grätzel, M. Redox targeting of insulating electrode materials: A new approach to high-energy-density batteries. *Angewandte Chemie - International Edition* **45**, 8197–8200 (2006).

42. Huang, Q., Li, H., Grätzel, M. & Wang, Q. Reversible chemical delithiation/lithiation of LiFePO4: Towards a redox flow lithium-ion battery. *Physical Chemistry Chemical Physics* **15**, 1793–1797 (2013).

43. Pan, F. *et al.* Redox Targeting of Anatase TiO2 for Redox Flow Lithium-Ion Batteries. *Adv Energy Mater* **4**, 1–7 (2014).

44. Qi, Z. & Koenig, G. M. Review Article: Flow battery systems with solid electroactive materials. *Journal of Vacuum Science & Technology B, Nanotechnology and Microelectronics: Materials, Processing, Measurement, and Phenomena* **35**, 040801 (2017).

45. Huang, Q., Yang, J., Ng, C. B., Jia, C. & Wang, Q. A redox flow lithium battery based on the redox targeting reactions between LiFePO 4 and iodide. *Energy Environ. Sci.* **9**, 917–921 (2016).

46. Zanzola, E. *et al.* Redox Solid Energy Boosters for Flow Batteries: Polyaniline as a Case Study. *Electrochim Acta* **235**, 664–671 (2017).

47. Páez, T., Martínez-Cuezva, A., Palma, J. & Ventosa, E. Mediated Alkaline Flow Batteries: From Fundamentals to Application. *ACS Appl Energy Mater* **2**, 8328–8336 (2019).

48. Chen, Y. *et al.* A Stable and High-Capacity Redox Targeting-Based Electrolyte for Aqueous Flow Batteries. *Joule* **3**, 2255–2267 (2019).

49. Zhou, M. *et al.* Single-Molecule Redox-Targeting Reactions for a pH-Neutral Aqueous Organic Redox Flow Battery. *Angewandte Chemie - International Edition* **59**, 14286–14291 (2020).

50. Tolmachev, Y. V. & Starodubceva, S. V. Flow batteries with solid energy boosters. *Journal of Electrochemical Science and Engineering* vol. 12 731–766 Preprint at https://doi.org/10.5599/jese.1363 (2022).

51. Reiss, H. The Fermi level and the redox potential. *J Phys Chem* **89**, 3783–3791 (2002).

52. Polcari, D., Dauphin-Ducharme, P. & Mauzeroll, J. Scanning Electrochemical Microscopy: A Comprehensive Review of Experimental Parameters from 1989 to 2015. *Chem Rev* **116**, 13234–13278 (2016).

53. Bard, A. J., Fan, F.-R. F., Kwak, J. & Lev, O. Scanning Electrochemical Microscopy. Introduction and Principles. *Anal Chem* **61**, 132–138 (1989).

54. Blair, E. O. Doctoral thesis: The Optimisation and Characterisation of Durable Microelectrodes for Electroanalysis in Molten Salt. (The University of Edinburgh, 2017). doi:https://era.ed.ac.uk/handle/1842/25671.

55. Bard, A. J. & Zoski, C. *Electroanalytical Chemistry A Series of Advances*. vol. 24 (CRC Press, 2012).

56. Bard, A. J. & Mirkin, M. V. *Scanning Electrochemical Microscopy, 2nd Edition. Scanning Electrochemical Microscopy, Second Edition* (CRC Press, 2012). doi:https://doi.org/10.1201/b11850.

57. Lefrou, C. & Cornut, R. Analytical Expressions for Quantitative Scanning Electrochemical Microscopy (SECM). *ChemPhysChem* **11**, 547–556 (2010).

58. Lin, T. E. *et al.* Multiple scanning electrochemical microscopy mapping of tyrosinase in micro-contact printed fruit samples on polyvinylidene fluoride membrane. *Electrochim Acta* **179**, 57–64 (2015).

59. Deng, H. *et al.* Kinetic differentiation of bulk/interfacial oxygen reduction mechanisms at/near liquid/liquid interfaces using scanning electrochemical microscopy. *Journal of Electroanalytical Chemistry* **732**, 101–109 (2014).

60. Tavakkoli, M. *et al.* Mesoporous Single-Atom-Doped Graphene–Carbon Nanotube Hybrid: Synthesis and Tunable Electrocatalytic Activity for Oxygen Evolution and Reduction Reactions. *ACS Catal* **10**, 4647–4658 (2020).

61. Cornut, R. & Lefrou, C. A unified new analytical approximation for negative feedback currents with a microdisk SECM tip. *Journal of Electroanalytical Chemistry* **608**, 59–66 (2007).

62. Cornut, R. & Lefrou, C. New analytical approximation of feedback approach curves with a microdisk SECM tip and irreversible kinetic reaction at the substrate. *Journal of Electroanalytical Chemistry* **621**, 178–184 (2008).

63. Lefrou, C. A unified new analytical approximation for positive feedback currents with a microdisk SECM tip. *Journal of Electroanalytical Chemistry* **592**, 103–112 (2006).

64. Janoschka, T., Martin, N., Hager, M. D. & Schubert, U. S. An Aqueous Redox-Flow Battery with High Capacity and Power: The TEMPTMA/MV System. *Angewandte Chemie International Edition* **55**, 14427–14430 (2016).

65. Ma, F., Li, Q., Wang, T., Zhang, H. & Wu, G. Energy storage materials derived from Prussian blue analogues. *Sci Bull (Beijing)* **62**, 358–368 (2017).

66. Goda, E. S., Lee, S., Sohail, M. & Yoon, K. R. Prussian blue and its analogues as advanced supercapacitor electrodes. *Journal of Energy Chemistry* vol. 50 206–229 Preprint at https://doi.org/10.1016/j.jechem.2020.03.031 (2020).

67. Xu, Y. *et al.* Prussian blue and its derivatives as electrode materials for electrochemical energy storage. *Energy Storage Mater* **9**, 11–30 (2017).

68. Lu, Y., Wang, L., Cheng, J. & Goodenough, J. B. Prussian blue: A new framework of electrode materials for sodium batteries. *Chemical Communications* **48**, 6544–6546 (2012).

69. Wessells, C. D., Huggins, R. A. & Cui, Y. Copper hexacyanoferrate battery electrodes with long cycle life and high power. *Nat Commun* **2**, 2–6 (2011).

70. Kanninen, P. *et al.* Carbon corrosion properties and performance of multi-walled carbon nanotube support with and without nitrogen-functionalization in fuel cell electrodes. *Electrochim Acta* **332**, 1–11 (2020).

71. Wagner, C. & Traud, W. *On the Interpretation of Corrosion Processes Through the Superposition of Electrochemical Partial Processes and on the Potential of Mixed Electrodes, with a Perspective by F. Mansfeld.* https://doi.org/10.5006/1.3279894 (1938).

72. Jin, S. *et al.* Near Neutral pH Redox Flow Battery with Low Permeability and Long-Lifetime Phosphonated Viologen Active Species. *Adv Energy Mater* **10**, 2000100 (2020).

73. Merryweather, A. J., Schnedermann, C., Jacquet, Q., Grey, C. P. & Rao, A. Operando optical tracking of single-particle ion dynamics in batteries. *Nature* **594**, 522–528 (2021).

74. Xu, C. *et al.* Operando visualization of kinetically induced lithium heterogeneities in single-particle layered Ni-rich cathodes. *Joule* **6**, 2535–2546 (2022).

75. Redor, S. *et al.* Electrochromic Corundum-like Compound Based on the Reversible (De)insertion of Lithium: Li2Ni2W2O9. *J Am Chem Soc* **145**, 12823–12836 (2023).

76. Wei, W. *et al.* Accessing the Electrochemical Activity of Single Nanoparticles by Eliminating the Heterogeneous Electrical Contacts. *J Am Chem Soc* **142**, 14307–14313 (2020).

77. Yuan, T., Wei, W., Jiang, W. & Wang, W. Vertical Diffusion of Ions within Single Particles during Electrochemical Charging. *ACS Nano* **15**, 3522–3528 (2021).

78. Niu, B. *et al.* Determining the depth of surface charging layer of single Prussian blue nanoparticles with pseudocapacitive behaviors. *Nat Commun* **13**, (2022).

79. Jiang, W. *et al.* Tracking the optical mass centroid of single electroactive nanoparticles reveals the electrochemically inactive zone †. **12**, 8556–8562 (2021).
80. Evans, R. C., Nilsson, Z. N. & Sambur, J. B. High-Throughput Single-Nanoparticle-Level Imaging of Electrochemical Ion Insertion Reactions. *Anal Chem* **91**, 14983–14991 (2019).
81. Colby Evans, R., Ellingworth, A., Cashen, C. J., Weinberger, C. R. & Sambur, J. B. Influence of single-nanoparticle electrochromic dynamics on the durability and speed of smart windows. *Proc Natl Acad Sci U S A* **116**, 12666–12671 (2019).
82. Komayko, A. I., Arkharova, N. A., Presnov, D. E., Levin, E. E. & Nikitina, V. A. Resolving the Seeming Contradiction between the Superior Rate Capability of Prussian Blue Analogues and the Extremely Slow Ionic Diffusion. *Journal of Physical Chemistry Letters* **13**, 3165–3172 (2022).

**TURUN
YLIOPISTO**
UNIVERSITY
OF TURKU